



Synthesis, Characterization, and Bioactivity of a Tridentate Nitrogen–Sulfur Schiff Base Derived from Carbothioamide and Its (Fe, Co, Cu, Cd) Metal Complexes: DFT, Molecular Docking, and Biomedical Applications

Mohammed M. Abduljawad*, M .S .A. Mansour, Rifaat H. Hilal, Ahmed A. El-Sherif

Chemistry Department, Faculty of Science, Cairo University, Giza, 12613 Egypt



Abstract

This investigation presents a detailed examination of transition metal complexes derived from a recently synthesized Carbothioamide Schiff Base Ligand, denoted as (Z)-2-((E)-1-(2-(4-chlorophenyl)hydrazineylidene)propan-2-ylidene)-N-phenylhydrazine-1-carbothioamide or (ZHC), known for its biological potency. The synthesis involved condensation of (E)-1-(2-(4-chlorophenyl)hydrazineylidene)propan-2-one with N-phenylhydrazinecarbothioamide to yield the Schiff base ligand (ZHC). The (ZHC) and its metal complexes have been thoroughly analyzed using several techniques, including Elemental analysis, UV-visible spectroscopy, FT-IR, Mass spectrometry, and conductometry measurements. Density functional theory (DFT) calculations estimated their electronic properties, such as energy gaps and dipole moments, suggesting a distorted octahedral geometry. Additionally, Molecular Electrostatic Potential (MEP) calculations at the DFT level were correlated with experimental data. The complexes showed promising antimicrobial activity against a range of bacterial and fungal strains. The Cd (II) complex exhibited the highest efficacy against all tested organisms. Furthermore, the antitumor potential of the complexes against MCF-7 (Breast carcinoma) cells was evaluated with the [Cd(ZHC)Cl₂(H₂O)]·H₂O complex demonstrating superior activity (IC₅₀ value of 10µg/ml) compared to cisplatin. Importantly, it exhibited reduced cytotoxicity towards normal cells (VERO cells) compared to cisplatin. Molecular docking, utilizing DFT-optimized configurations of the (ZHC) and its Cd (II) complex, provided insights into their interactions with specific protein structures (3QX3 and 6XBH) associated with specific cellular targets, namely MCF cells and the COVID-19 virus protein. The analysis of the docking study offers valuable structural insights for potential inhibition studies. This comprehensive study underscores the synthesized compounds' multifaceted applications and promising bioactive properties.

KEYWORDS: Schiff base complexes; Carbothioamides; spectral studies; spectra Molecular docking; DFT; Antimicrobial activity; Anti-COVID-19

1. Introduction

Schiff bases, first reported by Hugo Schiff in 1864, are versatile organic compounds characterized by an azomethine functional group (-C=N-) [1]. These compounds, formed through the condensation of primary amines with aldehydes or ketones, have garnered significant attention in coordination chemistry due to their ability to form stable complexes with various metal ions. Schiff base metal complexes exhibit a wide range of properties and applications across multiple fields, including medicinal chemistry, catalysis, and materials science [2]. Thiosemicarbazones are a significant category of organic compounds characterized by an -NH-C(=S)NH-N= bond. These compounds serve as versatile intermediates in the synthesis of various molecular entities. Notably, thiosemicarbazones exhibit diverse medicinal properties and biological activities, including but not limited to anticancer [3], antiviral [4], antimicrobial [3], antibacterial [5], and antioxidant effects [7–11]. The pivotal role of nitrogen (N) and sulfur (S) atoms in metal coordination at active sites within numerous metalloproteins is well-established [12]. They explored organic ligands featuring heteroatoms as coordination sites, which has emerged as a prominent avenue within coordination chemistry, presenting a rich array of intriguing and practically applicable complexes. Specifically, ligands endowed with multiple donor heteroatoms have garnered widespread attention globally owing to their robust chelating capabilities that facilitate the formation of mono-, di-, or multinuclear complexes [13, 14]. Furthermore, the active lone pair of electrons associated with these heteroatoms significantly contributes to the bonding dynamics in metal-ligand interactions. Schiff bases, distinguished by the existence of an azomethine functional group, exhibit a propensity to establish chelating rings through coordination with transition metals. This unique characteristic contributes to their diverse

*Corresponding author e-mail: mohammedabduljawad83@gmail.com (Mohammed M. Abduljawad).

Received date 10 August 2024; revised date 26 September 2024; accepted date 02 October 2024

DOI10.21608/ejchem.2024.311195.10172

©2025 National Information and Documentation Center (NIDOC)

biological and medicinal attributes [15-19], encompassing antimicrobial, anti-inflammatory, antibacterial, antifungal, and anticancer properties. Density Functional Theory (DFT) has emerged as a powerful computational method for investigating the electronic structure and properties of molecules and materials, including Schiff base metal complexes [1-3]. This quantum mechanical approach offers a balance between accuracy and computational efficiency, making it particularly useful for studying large molecular systems. In the context of Schiff base metal complexes, DFT calculations provide valuable insights into various aspects of their structure and reactivity. It helps determine the most stable molecular configurations, offering precise information about bond lengths, angles, and overall structural parameters. DFT allows for the calculation of HOMO-LUMO energy gaps, electron density distributions, and molecular orbital compositions, which are crucial for understanding reactivity and spectroscopic properties [1-5]. By computing energy profiles for different reaction pathways, DFT assists in elucidating reaction mechanisms and transition states. DFT-calculated molecular electrostatic potential (MEP) maps provide visual representations of charge distributions, helping to identify potential reactive sites [1, 2]. MEP is particularly valuable in coordination chemistry and drug design, complementing other molecular descriptors to enhance understanding of electronic structure and reactivity. This technique finds wide application in medicinal chemistry, materials science, and catalysis, guiding the design of new compounds and the interpretation of experimental results. In the context of Schiff base metal complexes, docking studies provide valuable insights into their potential biological activities and mechanisms of action [1-8]. This approach simulates the orientation and conformation of a ligand within a protein's binding site, allowing researchers to evaluate the strength and nature of molecular interactions. The primary aim of this investigation is to synthesize an innovative Schiff base ligand (denoted as **ZHC**) through the condensation process involving (E)-1-(2-(4-chlorophenyl) hydrazineylidene) propan-2-one and N-phenylhydrazinecarbothioamide. Subsequently, the focus extends to the development of complexes with Fe (III), Co (II), Cu (II), and Cd (II), achieved through rigorous physicochemical techniques for thorough characterization. The research extends to exploring the biological activities of the Schiff base and its metal complexes, encompassing antibacterial, antifungal, and anticancer properties. To delve into the molecular interactions, molecular docking studies have been conducted, shedding light on the potential binding modes of the (**ZHC**) and its Cd (II) complex with active sites on various receptors (**3QX3** and **6XBH**). The docking analyses were meticulously carried out using MOE software, which was recognized for its robust capabilities in rigid molecular docking.

2. Experimental Procedures and Methodological Approaches

2.1. Experimental Procedure

2.1.1. Reagents and Chemical Compounds.

In this investigation, we employed chemicals characterized by high purity, including (E)-1-(2-(4-chlorophenyl) hydrazineylidene) propan-2-one and N-phenylhydrazinecarbothioamide, sourced from Merck; FeCl₃·6H₂O obtained from SigmaAldrich; and CoCl₂·6H₂O, CuCl₂·2H₂O, and CdCl₂·2H₂O procured from BDH. Absolute Ethanol, an organic solvent of spectroscopic purity, was acquired from BDH. All preparations consistently used bidistilled water obtained from glass apparatuses. The MCF-7 human tumor cell line, stored at -180°C in liquid nitrogen, was procured from the American Type Culture Collection. Cultivation and maintenance of the MCF-7 tumor cell line were executed at the National Cancer Institute in Cairo, Egypt, through successive sub-culturing.

2.1.2. Solutions

Stock solutions of (**ZHC**) and its metal complexes, each at a concentration of 1×10^{-3} M, were meticulously formulated by dissolving the appropriate amounts in N, N-dimethylformamide for the Cu (II) complexes, and in ethanol for (**ZHC**), Fe (III), Co (II), and Cd (II) complexes. The electrical conductivity of the 1×10^{-3} M metal complex solutions was subsequently measured. Following this, diluted solutions of (**ZHC**) and its metal complexes, with a concentration of 1×10^{-4} M, have been precisely formulated as a result of diluting the previously established stock solutions for UV-Vis spectral analysis.

2.1.3. Anticancer Analysis Solution Preparation and Protocol

A stock solution of (**ZHC**) has been freshly prepared in 90% ethanol at a concentration of 1×10^{-3} M. Dimethyl sulfoxide (DMSO) has been used for cell cryopreservation. RPMI-1640 medium, supplemented with sodium bicarbonate, has been prepared, sterilized through a 0.22 μ m filter, and stored at 4°C. Before use, the medium was warmed to 37°C and enriched with penicillin-streptomycin and fetal bovine serum (FBS). A 0.05% isotonic trypan blue solution has been prepared in normal saline for cell viability assessment. Cells were harvested with 0.025% trypsin, and unbound SRB dye was removed using 1% acetic acid. The SRB dye has been dissolved in 1% acetic acid at a concentration of 0.40%. A 50% trichloroacetic

acid (TCA) solution was prepared, and 50 μL of it was added to 200 μL of RPMI-1640 medium per well for protein precipitation. Isopropanol (100%) and ethanol (70%) have been used in the procedures. The SRB dye has been solubilized in a 10 mM Tris base solution with a pH of 10.50, adjusted with 2 M hydrochloric acid.

2.1.4. Instrumentation

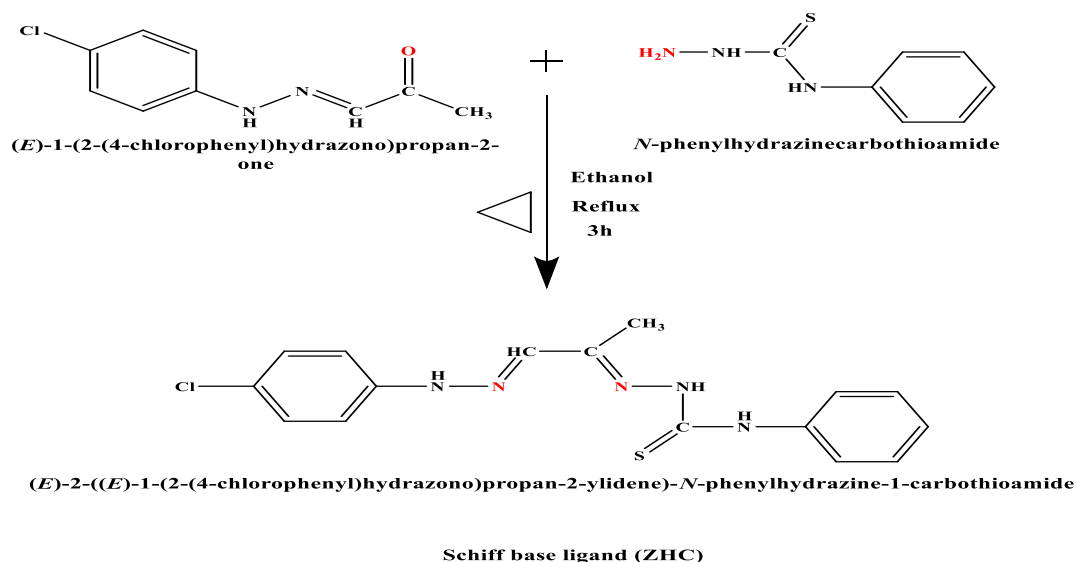
The synthesized metal complexes have been analyzed employing a variety of analytical techniques. Elemental analysis (CHN) has been carried out at Cairo University with a CHNS-932 analyzer to determine carbon, hydrogen, and nitrogen content. Melting points have been verified using a Triforce XMTD-3000 instrument. Metal content analysis has been conducted using inductively coupled plasma atomic absorption spectrometry (ICP-AAS) at the Egyptian Petroleum Research Institute. Fourier transform infrared (FT-IR) spectroscopy was performed on a PerkinElmer 1650 spectrometer with KBr pellets in the 4000–400 cm^{-1} range. The molar conductivity of 10^{-3} M complex solutions in dimethylformamide (DMF) has been measured using a Jenway 4010 conductivity meter. Proton nuclear magnetic resonance (^1H NMR) spectra were recorded in DMSO-d_6 with a tetramethylsilane reference on a 300 MHz Varian-Oxford Mercury instrument at room temperature. Electron ionization mass spectrometry (EI-MS) at 70 eV was conducted using an MS-5988 instrument. Thermogravimetric analysis (TGA/DTG) from room temperature to 1000°C was carried out utilizing a Shimadzu TG-50H analyzer. UV-Vis spectrophotometry has been performed in the 200–700 nm range on a PerkinElmer Lambda 20 spectrometer. Anticancer testing was conducted at Cairo University's National Cancer Institute, while antimicrobial assessments have been performed at Cairo University's Microanalytical Center.

2.2. Preparation of ZHC and its metal complexes.

Elemental analyses were performed on the novel (ZHC) ligand. Table 1 presents the outcomes of these analyses, encompassing nitrogen (N), hydrogen (H), and carbon (C) in conjunction with the melting points. The acquired results align with the calculated values from the proposed molecular formula. The observed distinct melting points attest to the prepared (ZHC) purity and its complexes. The synthetic route for the (ZHC) is delineated in Scheme 1. Furthermore, the structural confirmation of this (ZHC) is affirmed through detailed analyses of infrared (IR) and proton nuclear magnetic resonance (^1H NMR) spectra, with an elaborate discussion reserved for the metal complexes [20]. The (ZHC) exhibits a distinctive brown color and maintains stability at room temperature, demonstrating solubility in dimethyl sulfoxide (DMSO) solvent. The congruence between the obtained results and those derived from the proposed formula underscores the reliability of the experimental data. Scheme 1 illustrates the structural configuration of the (ZHC). Evaluation of the metal-to-ligand ratio across all complexes, determined by assessing carbon, hydrogen, nitrogen, and metal content, suggests a 1:1 ratio (Table 1), following an (M):(ZHC) configuration. Experimental elemental analyses for the complexes closely align with theoretical data, validating the proposed formula (Table 1) [21]. Characterization of the tridentate ligand (ZHC) metal complexes incorporates diverse analytical techniques, including elemental analyses, molar conductivity, infrared spectroscopy (IR), proton nuclear magnetic resonance (^1H NMR), ultraviolet-visible spectroscopy (UV–Vis), mass spectrometry, and thermal analyses. The suggested structures are depicted in Fig 1.

2.2.1. Synthesis of (ZHC) Ligand

The synthesis of the (ZHC) was accomplished using the prescribed procedure. The method involved the condensation of (E)-1-(2-(4-chlorophenyl)hydrazineylidene)propan-2-one (1.525 mmol, 0.3 g) and N-phenylhydrazinecarbothioamide (1.525 mmol, 0.255 g) in heated 100% ethanol at 60 °C. The reaction mixture underwent reflux for 4 hours. Following the evaporation of ethanol, filtration, and recrystallization of the resultant orange solid, the pure Schiff base was obtained with a satisfactory yield of 83%. Scheme (1) provides an illustrative depiction of the (ZHC) structure and the associated formation reaction. With a yield of 87%, yellowish-brown solid crystalline material was obtained with a melting point of 138°C. Elemental analysis yielded the following results for $\text{C}_{16}\text{H}_{16}\text{ClN}_5\text{S}$ (%): C, 55.57; H, 4.66; Cl, 10.25; N, 20.25; S, 9.27. Experimental analysis found (%): C, 55.35; H, 4.41; Cl, 10.02; N, 20.07; S, 9.04. Infrared spectroscopy (IR) revealed absorption peaks at 3308 cm^{-1} (NH stretching), 1595 cm^{-1} (C = N stretching), and 1512 cm^{-1} ($\nu(\text{C}=\text{S})$ vibration). Additionally, UV–visible spectroscopy exhibited absorption bands at 310 nm ($\pi\text{--}\pi^*$ transition), 329 nm ($n\text{--}\pi^*$ transition), and 379 nm (charge transfer).



Scheme 1. (ZHC) synthesis Pathway

2.2.2 Synthesis of Binary (ZHC) Complexes

The synthesis of Fe (III), Co (II), Cu (II), and Cd (II) complexes involved the reaction between a 1:1 molar combination of a hot ethanolic solution (at 60 °C) containing 0.86 mmol of metal chloride and 0.3 g (0.86 mmol) of the (ZHC). The resulting mixed solution underwent refluxing for 4 hours, leading to the precipitation of the complexes. Filtration was employed for collection, and subsequent purification was achieved through multiple washes with diethyl ether. Scheme (2) illustrates the structure of the binary (ZHC) metal complexes and outlines the formation reaction.

2.2.2.1. [Fe(ZHC)Cl₃]·2H₂O

The compound was synthesized with a yield of 81%, presenting as a dark brown solid with a melting point of 213°C. Elemental analysis yielded the following calculated percentages for (C₁₆H₁₈Cl₃FeN₅O₃S): C, 36.53; H, 3.45; Cl, 26.96; Fe, 10.62; N, 13.31; S, 6.09. Experimental findings deviated slightly with measured C, 36.37; H, 3.24; Cl, 26.78; Fe, 10.51; N, 13.04; S, 5.85. The compound exhibited a molar conductivity (Λ_m) of 32 $\Omega^{-1} \text{ mol}^{-1} \text{ cm}^2$. The FT-IR spectrum displayed characteristic peaks at 3294 cm^{-1} (NH stretching), 1606 cm^{-1} (Azomethine C=N), 1491 cm^{-1} (C=S), 405 cm^{-1} (M-S), 458 cm^{-1} (M-N), and 329 cm^{-1} (M-Cl). UV-Vis spectroscopy revealed absorption maxima at 210 nm (π - π^* transition), 260 nm (conjugated π - π^* transition), and 285 nm (n- π^* transition). The data collectively suggest the successful synthesis of the compound with distinct spectroscopic features.

2.2.2.2. [Co (ZHC)(H₂O)Cl₂]·2H₂O

The compound was obtained with a yield of 84%, presenting as a dark brown solid crystal with a melting point of 235°C. Elemental analysis was performed, and the calculated percentages for (C₁₆H₂₂Cl₃CoN₅O₃S) were found to be C 36.28%, H 4.19%, Cl 20.08%, Co 11.13%, N 13.22%, and S 6.05%. Experimental values differed slightly, with C 36.09%, H 4.01%, Cl 19.88%, Co 10.95%, N 12.88%, and S 5.82%. The molar conductivity (Λ_m) was 27 $\Omega^{-1} \text{ mol}^{-1} \text{ cm}^2$. The compound exhibited characteristic peaks in the FT-IR spectrum at 3281 cm^{-1} (NH stretching), 1599 cm^{-1} (azomethine C=N), 1493 cm^{-1} (C=S), 407 cm^{-1} (metal-sulfur, M-S), 465 cm^{-1} (metal-nitrogen, M-N), and 337 cm^{-1} (metal-chlorine, M-Cl). UV-Vis spectroscopy revealed absorption peaks at 209 nm, 217 nm, and 262 nm (π - π^* transitions), 285 nm (conjugated π - π^* transition), 295 nm (n- π^* transition), and 362 nm (charge transfer). In summary, the synthesis yielded a dark brown crystalline compound with distinct spectral features, and the elemental analysis provided insights into its composition. At the same time, spectroscopic data characterized its molecular structure and electronic transitions.

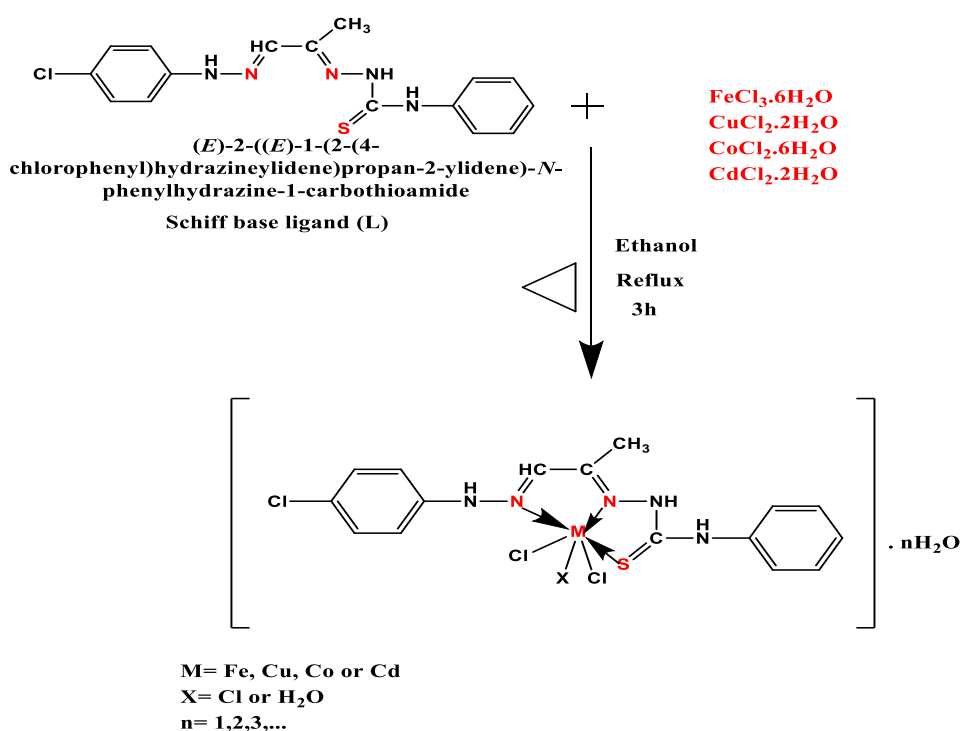
2.2.2.3. [Cu(ZHC)(H₂O)Cl₂]·2H₂O

The synthesis of the compound yielded 78%, resulting in the formation of dark brown solid crystals with a melting point of 247°C. The elemental analysis was performed, and the calculated values for (C₁₆H₂₂Cl₃CuN₅O₃S) were as follows: C, 35.97; H, 4.15; Cl, 19.90; Cu, 11.89; N, 13.11; S, 6.005. Experimental analysis yielded slightly different values: C, 35.67; H, 4.02; Cl, 19.68; Cu, 11.52; N, 13.00; S, 5.85. The compound exhibited a molar conductivity (Λ_m) of 19 $\Omega^{-1} \text{ mol}^{-1} \text{ cm}^2$.

Fourier-transform infrared spectroscopy (FT-IR) revealed characteristic peaks at 3291 cm^{-1} for NH stretching, 1618 cm^{-1} for azomethine C=N stretching, 1490 cm^{-1} for C=S stretching (with a shoulder), 397 cm^{-1} for M–S stretching, 463 cm^{-1} for M–N stretching, and 318 cm^{-1} for M–Cl stretching (weak). The UV–Vis spectrum displayed absorption peaks at 212 nm, 220 nm, and 273 nm, indicative of π – π^* transitions, along with additional peaks at 293 nm (conjugated π – π^*), 328 nm (n – π^*), and 397 nm (charge transfer).

2.2.2.4. $[\text{Cd}(\text{ZHC})(\text{H}_2\text{O})\text{Cl}_2]\cdot\text{H}_2\text{O}$

A dark red-black crystalline solid with a melting point of 285°C was synthesized with a yield of 82%. The molecular formula, $(\text{C}_{16}\text{H}_{20}\text{CdCl}_3\text{N}_5\text{O}_2\text{S})$, was characterized through elemental analysis, with calculated and found percentages as follows: C (34.00% vs. 33.87%), H (3.57% vs. 3.34%), Cd (19.89% vs. 19.61%), Cl (18.82% vs. 18.57%), N (12.39% vs. 12.09%), and S (5.67% vs. 5.33%). The compound exhibited a molar conductivity (Λm) of $37\ \Omega^{-1}\text{ mol}^{-1}\text{ cm}^2$. Infrared spectroscopy (FT-IR) revealed characteristic peaks at 3279 cm^{-1} (NH stretching), 1613 cm^{-1} (Azomethine C=N), 1489 cm^{-1} (C=S), 391 cm^{-1} (metal-sulfur, M–S), 457 cm^{-1} (metal-nitrogen, M–N), and 325 cm^{-1} (metal-chlorine, M–Cl). UV-Vis spectroscopy displayed absorption bands at (244 nm π – π^* transitions), 309 nm (π – π^* conjugated transitions), 323 nm (n – π^* transition), and 366 nm (charge transfer).



Scheme 2. (ZHC) metal complexes formation

2.2.3. Exploration of Spectrophotometric Analyses

Absorption spectra have been recorded for solutions containing the unbound (ZHC) and its metal complexes, each maintained at a concentration of $1 \times 10^{-4}\text{ M}$. The spectral analysis encompassed the wavelength range spanning 200 to 700 nm [1, 2].

2.2.4. Computational methodology

The electronic structure calculations of the (ZHC) and its Cd (II) complex have been executed using the Gaussian09 software package, as detailed in references [21, 22]. The structures underwent full optimization through density functional theory (DFT), employing the hybrid B3LYP functional. A mixed basis set approach was adopted to represent all atoms within the system accurately. Specifically, the LANL2DZ basis set was utilized for the Cd atom, given its suitability for transition metals. For the ligand atoms (carbon, hydrogen, nitrogen, oxygen) in both the (ZHC) and its Cd (II) complex, the 6-31G(d,p) basis set was chosen, which is appropriate for the main group elements [22–24]. This strategic combination of basis sets facilitated the geometry optimization of the (ZHC) and its Cd (II) complex, enabling the calculation of various functional parameters such as Total Energy, Dipole Moment, E_{HOMO} , E_{LUMO} , Band Gap Energy ($\Delta E = E_{\text{HOMO}} - E_{\text{LUMO}}$), Electron Affinity,

Electronegativity, and Electrostatic Maps (MEP) [23]. The optimized molecular electrostatic potential (MEP) maps provided insights into the reactive sites within the molecules. Regions of electrophilic reactivity, characterized by negative potential, were illustrated in red, whereas areas of nucleophilic reactivity, marked by positive potential, were shown in blue. These MEP maps are crucial for understanding the reactivity and interaction patterns of the molecules, offering a visual representation of how they might behave in various chemical environments [1, 2].

2.2.5. Pharmacology

2.2.5.1. Antimicrobial efficacy

The investigation into the antimicrobial efficacy of the analyzed compounds utilized the agar well diffusion technique [25]. In vitro assessments of antibacterial properties encompassed Gram-positive bacterial strains, specifically *Staphylococcus aureus* (ATCC: 13565) and *Streptococcus mutans* (ATCC: 25175), as well as negative Gram bacteria, including *Escherichia coli* (ATCC: 10536) and *Klebsiella pneumoniae* (ATCC: 10031). These evaluations were performed on a nutrient agar medium. Antifungal activity was evaluated using a methodology detailed in prior research [26]. *Candida albicans* (ATCC: 10231) and *Aspergillus niger* (ATCC: 16404) were the fungal strains tested, employing Sabouraud dextrose agar medium. Comparative analysis was facilitated using standard drugs, namely Ampicillin and Gentamicin for (+Ve) and (-Ve) Gram bacteria, respectively, and Nystatin for fungal strains. The negative control involved the use of DMSO as the solvent. The compounds were tested at a 15 mg/ml concentration against both bacterial and fungal strains. Agar-based methodologies such as E-testing and disc diffusion were considered, as they offer expeditious and facile assessments compared to broth-based techniques [27].

2.2.5.2. Method of testing

Sterile culture media, approximately 20-25 mL per Petri dish, was poured and allowable to solidify at ambient temperature. A microbial suspension matching the McFarland 0.5 standard solution (1.5×10^5 CFU mL⁻¹) has been prepared in sterile saline, with turbidity adjusted to OD= 0.13 at 625 nm using a spectrophotometer [28]. Subsequently, within a 15-minute of turbidity adjustment, a sterile cotton swab was immersed in the prepared suspension and evenly spread on the desiccated agar surface. The swab was air-dried for 15 minutes with the lid secured. Using a sterile borer, wells of 6 mm diameter were created in the solidified media [28]. Then, 100 µL of the test compound solution was meticulously added to each well via a micropipette. The Petri dishes were then incubated at 37°C for 24 hours to assess antibacterial activity. This experimental procedure was replicated three times, and the inhibition zones were quantified in millimeters [28].

2.2.5.3 Anticancer efficacy

The (ZHC) and its metal complexes underwent cytotoxicity testing utilizing the Skehan and Storeng method [29]. Preceding the therapeutic intervention, 24 hours were allocated for compound dilutions (12.5, 25, 50, and 100 µg/ml) within a 96-well plate, facilitating compound attachment to the cellular platform. Subsequently, monolayer cells, including the compounds, have been incubated for 48 hours at 37°C with 5% CO₂. Post-incubation, cells have been fixed, washed, and subjected to SRB staining. The excess stain was eliminated with Tris-EDTA buffer and acetic acid, and the stain was then recovered. All specimens' optical density (OD) has been measured at 564 nm using an ELISA microplate reader. Background corrections were automatically applied, and mean values were computed for each drug concentration. The correlation between drug concentration and surviving fraction was delineated, generating survival curves for each substance in the breast Cancer cell line. The control group comprised untreated MCF-7 breast cancer cell lines, while the positive control group included MCF7 breast cancer cell lines treated with the standard drug Cisplatin. Upon protocol completion, the survival curves provided insights into the impact of different substances on breast Cancer cell lines. A correlation was established between the surviving fraction and the concentration of the administered drug to evaluate the influence of the compounds on cellular viability. This process generated a survival curve for the breast cancer cell line under investigation. The percentage of cell survival was determined using the following formula:

$$\text{Survival fraction} = \text{O.D. of treated cells} / \text{O.D. of control cells}$$

The principal objective of this investigation was to determine IC₅₀ values indicative of the concentrations of the (ZHC) or its metal complexes necessary to inhibit cell growth by 50%. The entire experimental procedure was rigorously replicated thrice specifically for the MCF7 cell line, aiming to enhance the outcomes' dependability and uniformity.

2.2.6. Molecular Docking Investigation

Molecular docking investigations have been executed using MOE 2014 software, renowned for its adeptness in rigid molecular docking [1, 2]. These analyses played a pivotal role in prognosticating potential binding modes of the (**ZHC**) and its selected binary Cd (II) complex, owing to their heightened biological activity against significant receptors. Specifically, the study targeted crystal structures of vital receptors, including Human topoisomerase IIbeta in complex with DNA and etoposide (**PDB ID: 3QX3**), integral components associated with cancer treatment [30], and the Main Protease (Mpro) of SARS-CoV-2, a pivotal antiviral drug target, represented by the Crystal structure of the SARS-CoV-2 (COVID-19) main protease in complex with inhibitor UAW247 (**PDB ID: 6XBH**) [31]. The software necessitated input in PDB format, encompassing the (**ZHC**), the binary Cd (II) complex, and the receptors. During the preparation of input files, extraneous elements such as water molecules, co-crystallized ligands, and unsupported components like Na, K, Hg, etc., have been excluded. However, amino acid chains were retained for subsequent analysis [32]. The (**ZHC**) and its selected binary Cd (II) complex were generated in PDB file format using Gaussian software. Crystal structures of all receptors have been sourced from the Protein Data Bank (PDB) and are available at <http://www.rcsb.org/pdb>. This methodology reveals the ligand-receptor site and the nature of interactions, estimating the distance between the studied compounds and the receptor within the interaction grid. The scoring energy of each pose, simulated by the docking computations, shows the extent of the inhibitory effect of the corresponding compounds. This analysis yields valuable insights into potential therapeutic applications. In summary, this research employed a well-established methodology to evaluate the cytotoxic potential of the (**ZHC**) and its Cd (II) metal complex. It utilized a spectrum of concentrations and analytical techniques to assess their impact on the growth of breast cancer cells. The calculation of IC₅₀ values served as a gauge for the efficacy of these compounds in inhibiting cell growth, and the experiment underwent rigorous replication to enhance the scientific robustness of the findings.

3. RESULTS AND DISCUSSION

The (**ZHC**) and their corresponding metal complexes underwent a comprehensive characterization process, encompassing elemental analysis, molar conductance, UV-visible spectroscopy, Fourier-Transform Infrared (FT-IR) spectroscopy, Mass spectrometry, ¹H Nuclear Magnetic Resonance (NMR) spectroscopic analysis, and Thermal analysis studies, specifically Thermogravimetric Analysis (TG) and Derivative Thermogravimetry (DTG). The findings of these investigations are succinctly summarized sequentially.

3.1. Schiff base ligand (**ZHC**) Characterization

The elemental analysis outcomes revealed that the synthesized ligand, denoted as (**ZHC**), which is a 2-((Z)-2-((E)-1-(2-(4-chlorophenyl)hydrazineylidene)propan-2-ylidene)-N-phenylhydrazine-1-carbothioamide), demonstrated close conformity with the calculated values for carbon (C), hydrogen (H), and nitrogen (N). The ascertained molecular formula for the ligand was found to be **C₁₆H₁₆ClN₅S**, aligning with the proposed formula. At room temperature, (**ZHC**) manifested as a stable yellowish-brown solid, exhibiting solubility in DMSO and DMF. The mass spectrum of (**ZHC**) substantiated its proposed formula, revealing a molecular ion (m/z) peak at 345.20 amu, supporting the ligand's composition as **C₁₆H₁₆ClN₅S** with an atomic mass of 345.85 amu. Various peaks corresponding to distinct fragments of the ligand were also documented. The ¹H NMR spectrum of (**ZHC**) showcased multiple signals for aromatic ring protons within the range of 7.088-7.629 ppm [33]. Furthermore, signals at 10.047 ppm, 10.654 ppm, and 10.830 ppm were attributed to the –NH proton signal detected as a singlet (1H) [34] (refer to Table 3). The confirmation of the (**ZHC**) synthesis was deduced from the absence of evidence for the NH₂ group. The (**ZHC**) infrared (IR) spectrum exhibited a distinctive band at 1595 cm⁻¹, confirming the presence of the azomethine group and substantiating the successful formation of the (**ZHC**) ligand [35]. The Density Functional Theory (DFT) analysis concurred with this observation, capturing the corresponding peak at 1642 cm⁻¹. The close concurrence between the experimentally observed and theoretically calculated frequencies validates the practical synthesis of the (**ZHC**), as depicted in Fig 1. Discrepancies between theoretical and experimental frequencies may stem from systematic errors, potentially associated with factors such as harmonicity or from considering gas-phase molecules in DFT calculations. To mitigate these potential errors, a correlation coefficient of 0.9648 for LAN2DZ was applied [36, 37], aiming to enhance the accuracy and reliability of the obtained results.

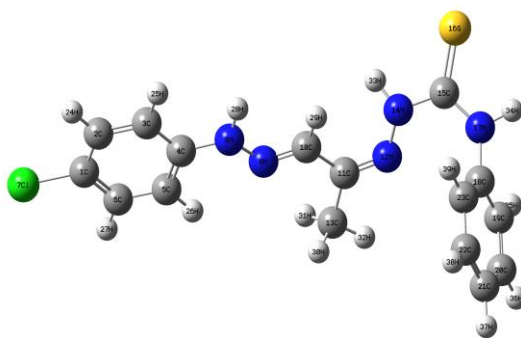


Fig 1. The optimized configuration of (ZHC)

3.2. Characterization of (ZHC) Metal complexes

3.2.1. Elemental analysis

The interaction between metal ions (iron, cobalt, copper, and cadmium) and (ZHC) resulted in the synthesis of metal complexes, yielding favorable results in a 1:1 metal-to-ligand ratio. These complexes demonstrated solubility in diverse organic solvents such as dimethylformamide (DMF) and dimethyl sulfoxide (DMSO). Comprehensive findings and data analysis are presented in Table 1. Consequently, the observed outcome forms a complex with stoichiometry denoted as (M): (ZHC).

Table 1: Comprehensive Analysis of Analytical and hysicochemical Properties of the (ZHC) and Its Corresponding Metal Complexes.

Cpds (chemical formula)	Color Yield (%)	M.p. (°C)	Found (Calc.)					Am (Ω^{-1} mol^{-1} cm^2)
			C (%)	H (%)	N (%)	S (%)	M (%)	
(ZHC)	yellowish brown 87%	138	55.35 (55.57)	4.41 (4.66)	20.07 (20.25)	9.04 (9.27)
[Fe(ZHC)Cl ₃]·H ₂ O	dark brown 81%	213	36.37 (36.53)	3.24 (3.45)	13.04 (13.31)	5.85 (6.09)	10.51 (10.62)	32
[Co(ZHC)(H ₂ O)Cl ₂]·2H ₂ O	dark brown 84%	235	36.09 (36.28)	4.01 (4.19)	12.88 (13.22)	5.82 (6.05)	10.95 (11.13)	27
[Cu(ZHC)(H ₂ O)Cl ₂]·2H ₂ O	dark brown 78%	247	35.67 (35.97)	4.02 (4.15)	13.00 (13.11)	5.85 (6.005)	11.52 (11.89)	19
[Cd(ZHC)(H ₂ O)Cl ₂]·H ₂ O	dark red- black 82%	285	33.87 (34.00)	3.34 (3.57)	12.09 (12.39)	5.33 (5.67)	19.61 (19.89)	37

3.2.2. Molar conductivity measurements

By employing the correlation ($\Lambda_m = K/C$), one can ascertain the molar conductance (Λ_m) of the complexes, where C represents the molar concentration of the solutions containing metal complexes. The new Schiff base ligand, denoted as (**ZHC**), serves as a tridentate ligand with a neutral nature. The chelates were dissolved in DEMSO, and the molar conductivities of solutions with a concentration of 10^{-3} M were measured at 25 ± 1 °C following the recommended procedure. The Fe (III), Cu (II), Co (II), and Cd (II) chelates exhibit molar conductance values ranging from 19 to $37 \Omega^{-1} \text{ mol}^{-1} \text{ cm}^2$ (Table 1). These observations suggest that these metal complexes are non-electrolytic, as the literature indicates [1, 2, 38, 39].

3.2.3. Mass spectral investigations

The mass spectrometry analyses of the metal complexes formed with the (**ZHC**) revealed distinctive molecular ion peaks, as detailed in Table 2. The examination of the mass spectral information confirmed the stoichiometric composition of the metal complex, represented as $[\text{M}(\text{ZHC})(\text{Cl})\text{m}(\text{H}_2\text{O})_n] \cdot x\text{H}_2\text{O}$. Moreover, the outcomes from these investigations aligned seamlessly with the anticipated molecular formulas, a correlation further supported by elemental analysis data (refer to Table 1)(supplementary Fig S1).

Table 2: Exploration of Extensive Datasets About (**ZHC**) and Its Respective Metal Complexes.

Compounds	m/z value		Interpretation
	Calculated	Found	
(ZHC)	345.85	345.20	$[\text{M}]^+$
(1) [Fe(ZHC)Cl3]·H2O	526.06	525.40	$[\text{M}]^+$
(2) [Co(ZHC)(H2O)Cl2]·2H2O	529.73	528.99	$[\text{M}]^+$
(3) [Cu(ZHC)(H2O)Cl2]·2H2O	534.35	535.80	$[\text{M}+1]^+$
(4) [Cd(ZHC)(H2O)Cl2]·H2O	565.19	565.90	$[\text{M}+1]^+$

3.2.4. ¹H NMR spectral investigations

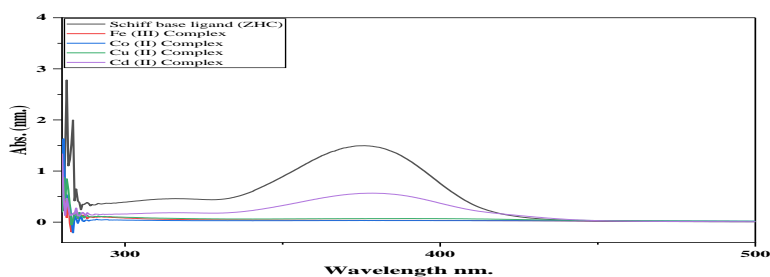
The proposed bonding arrangement in the synthesized complexes is substantiated through ¹H-NMR spectroscopic analysis. The ¹H-NMR spectra of the synthesized (**ZHC**) and its Cd (II) complex have been acquired in DMSO-d₆, and the corresponding chemical shift values (ppm) were determined. Within the ligand spectrum, multiplet signals in the range of 7.088-7.629 ppm were observed, corresponding to the aromatic phenol group, as detailed in the accompanying table. These signals were also discernible in the Cd(II) complex, manifesting at 7.181-7.817 ppm. Moreover, proton signals at 10.047 ppm, 10.654 ppm, and 10.830 ppm, attributed to the –NH proton signal detected as a singlet (1H) in (**ZHC**) [34] (refer to the table3), were identified. These signals persisted in the Cd (II) complex but shifted to higher values, registering at 10.525, 10.888, and 11.538 ppm, respectively. Additionally, the proton signals originating from the N-CH=N appeared as singlets at 7.817 ppm in the (**ZHC**). In the Cd (II) complex, these signals remained observable but experienced a shift to a higher value at 8.004 ppm, indicative of the chelation effect, as outlined in Table 3. The protons from the CH₃ group initially observed at 2.242 ppm in the Schiff base ligand, were still detectable at the same value in the Cd (II) complex. This observation implies that chelation occurred in the Cd (II) complex through the binding of Cd to both (C=N) and (C=S).

Table 3: ^1H NMR spectral data for the (ZHC) and its cadmium metal complexes.

Compounds	Chemical shift, (δ) ppm	Assignment
Schiff base ligand (ZHC)	10.047	(s, H, Cl-ph-NH)
	10.654	(s, H, ph-NH-C=S)
	10.830	(s, H, N-NH-C=S)
	7.088-7.629	(m, 10H, aromatic)
	7.817	(S, H, N-CH=N)
	2.42	(s, 3H, N=C-CH ₃)
[Cd(ZHC)(H ₂ O)Cl ₂]\cdot H ₂ O	10.525	(s, H, Cl-ph-NH)
	10.888	(s, H, ph-NH-C=S)
	11.538	(s, H, N-NH-C=S)
	7.181-7.817	(m, 10H, aromatic)
	8.004	(S, H, N-CH=N)
	2.42	(s, 3H, N=C-CH ₃)

3.2.5. UV-Visible Absorption Spectroscopy: Comparative Analysis

The UV-Vis spectra were acquired for the (ZHC) and its corresponding complexes under ambient conditions. The spectrum of (ZHC) exhibited a prominent absorption band at 310 nm, corresponding to the $\pi \rightarrow \pi^*$ transition of the Aromatic rings. Furthermore, a band emerged at 329 nm, indicating the $n \rightarrow \pi^*$ transition of the azomethine group, and a band at 379 nm denoted charge transfer. Upon coordination of the azomethine nitrogen to the metal centers, these bands underwent a shift to 209-273 nm for the $\pi \rightarrow \pi^*$ transition, 260-309 nm for conjugated $\pi \rightarrow \pi^*$, 285-323 nm for the $n \rightarrow \pi^*$ transition, and 362-366 nm for charge transfer [(1-3), (40-42)] (Fig2).

**Fig 2.** UV-Visible Absorption Spectra of ZHC and Its Metal Complexes

3.2.6. FT-IR spectral studies

The investigated complexes' infrared (IR) spectra were systematically analyzed compared to those of the unbound ligand, aiming to elucidate the degree of involvement of coordination sites in chelation, as summarized in Table 4 and Supplementary Fig S2. In the IR spectrum of the ligand (ZHC), a prominent band at 1595 cm^{-1} , corresponding to the azomethine $\nu(\text{C}=\text{N})$ group, was observed [43]. Notably, this specific band exhibited a noticeable shift to frequencies within the range of $1618\text{--}1633\text{ cm}^{-1}$ in the spectra of all the complexes, indicative of active participation of the azomethine nitrogen in coordination with the metal ions. The complexes' spectra displayed broad bands within the $3402\text{--}3434\text{ cm}^{-1}$ range, assigned to the

stretching vibration of the $\nu(\text{NH})$ group, suggesting the presence of coordinated water molecules [44]. The ligand's (**ZHC**) IR spectrum featured a 1512 cm^{-1} band associated with the $\nu(\text{C}=\text{S})$ group. Upon complex formation, this band shifted to frequencies within the $1489\text{--}1693\text{ cm}^{-1}$ range [45], signifying the coordination of nitrogen and sulfur from the Schiff base ligand with the metal ions [46]. Additionally, all complexes exhibited new bands in the spectral regions of $391\text{--}407\text{ cm}^{-1}$ (vibrational mode $\nu(\text{M-S})$), $318\text{--}337\text{ cm}^{-1}$ (vibrational mode $\nu(\text{M-Cl})$), and $457\text{--}465\text{ cm}^{-1}$ (vibrational mode $\nu(\text{M-N})$) [47–50]. The ligand (**ZHC**) demonstrated uninegative tridentate chelation, functioning as a chelating agent bonded to the metal ion through two nitrogen atoms from the azomethine group and one sulfur atom from the $(\text{C}=\text{S})$ of the Schiff base. The coordination of water molecules and a chlorine atom in all complexes led to the formation of octahedral complexes.

Table 4: "Predominant Infrared Spectral Bands of Binary Complexes Involving Isolated (**ZHC**) "

Compounds	ν [NH]	ν [C=N]	ν [C=S]	ν [M-N]	ν [M-S]	ν [M-Cl]
(ZHC)	3308 br	1595 sh	1512 m
(1) [Fe(ZHC)Cl ₃]·H ₂ O	3294 br	1626 sh	1491 m	458 w	405 w	329 w
(2) [Co(ZHC)(H ₂ O)Cl ₂]·2H ₂ O	3281 br	1618 w	1493 w	465 w	407 w	337 w
(3) [Cu(ZHC)(H ₂ O)Cl ₂]·2H ₂ O	3291 br	1628 sh	1490 w	463 w	397 w	318 w
(4) [Cd(ZHC)(H ₂ O)Cl ₂]·H ₂ O	3279 br	1633 sh	1489 sh	457 w	391 w	323 w

Sh=sharp, br=broad, w=weak.

3.2.7. Thermal analysis of Binary (**ZHC**) metal complexes

The study employed Thermal Gravimetric Analysis (TGA) to assess the thermal stability of synthesized metal complexes and differentiate between water molecules existing in a hydrated state or coordinated within their molecular structures [51, 52]. Thermal and Derivative Thermogravimetric analyses (TG and DTG) were performed on metal complexes formed with (**ZHC**) ligand, exploring their thermal behavior over a temperature range from ambient temperature to 800°C . The findings encompassed temperature intervals, stages of decomposition, product loss during decomposition, comparison of calculated and observed weight loss percentages, and residues of all compounds, as outlined in Table 5 and Fig 3. The thermal degradation kinetics of the complex [**Fe**(**ZHC**)Cl₃]·H₂O manifests a four-stage decomposition process, commencing at 35°C and culminating at 800°C and in the initial stage, spanning $35\text{--}100^\circ\text{C}$, dehydration occurs, reaching its zenith at 98°C , resulting in an experimentally observed weight loss of 3.15% (theoretically calculated as 3.42%). Subsequently, the second phase unfolds between $100\text{--}240^\circ\text{C}$, with a pinnacle at 200.34°C , marked by the expulsion of **C₇H₇N₂S**, yielding a mass loss of 28.56% (theoretical calculation: 28.74%). The third decomposition phase, spanning $240\text{--}325^\circ\text{C}$, is characterized by the liberation of **CH₃Cl₂**, leading to a weight loss of 16.19% (calculated as 16.33%), with the highest intensity observed at 305.39°C . Finally, the fourth decomposition stage, occurring in the $325\text{--}800^\circ\text{C}$ range, involves the release of **C₈H₆Cl₂N₃**, resulting in a weight loss of 40.589% (calculated as 40.88%), with peaks registered at 564.27 and 599.68°C . The residue after the complete degradation consists of metallic iron (Fe). The thermal degradation process of the compound [**Co**(**ZHC**)(H₂O)Cl₂]·2H₂O exhibits a three-step decomposition, commencing at 30°C and concluding at 800°C . The initial decomposition phase, occurring between $30\text{--}110^\circ\text{C}$, involves the elimination of **2H₂O**, evidenced by a peak at 97°C , resulting in an observed weight loss of 6.65% (calculated as 6.79%). Subsequently, the second step transpires from $110\text{--}305^\circ\text{C}$ with peaks at 112.5 , 225.8 , and 292.34°C , entailing the loss of **C₇H₉Cl₂N₂S** and an estimated mass loss of 41.85% (calculated as 42.31%). The final decomposition stage, transpiring within the $305\text{--}800^\circ\text{C}$ range, is characterized by the loss of the **C₉H₁₁CIN₃** molecule, resulting in a weight loss of 36.59% (calculated as 37.12%) with a peak at 591.68°C , ultimately leaving behind cobalt oxide (CoO) as the decomposition product. The thermal degradation kinetics of the compound [**Cu**(**ZHC**)(H₂O)Cl₂]·2H₂O exhibit a three-stage decomposition process, commencing at 30°C and concluding at 800°C . The initial stage, unfolding within the temperature range of $30\text{--}110^\circ\text{C}$, involves the dehydrative elimination of **2H₂O**, characterized by a peak at 92°C , resulting in an experimental weight loss of 6.308% (theoretical calculation: 6.73%). Subsequently, the second decomposition step transpires between $95\text{--}400^\circ\text{C}$, featuring peaks at 165.5 and 213.59°C , entailing the expulsion of **C₇H₈CIN** with an anticipated mass loss of 25.79% (calculated as 26.49%). The ultimate degradation stage, transpiring in the $400\text{--}800^\circ\text{C}$ range, is distinguished by the release of the **C₉H₁₀C₁₂N₄S** moiety, leading to a weight loss of 51.46% (theoretical calculation: 51.87%) with a peak observed at 463.39°C . The residue comprises cobalt oxide (**CuO**) as the

resultant decomposition product. The thermal degradation process of the complex $[\text{Cd}(\text{ZHC})(\text{H}_2\text{O})\text{Cl}_2]\cdot\text{H}_2\text{O}$ exhibits a multi-step decomposition sequence spanning the temperature range of 40 to 800 °C. In the initial stage, occurring between 40 and 120 °C, dehydration takes place, resulting in the liberation of water with a discernible peak at 98 °C, causing an experimental weight loss of 2.79% (theoretical 3.18%). Subsequently, the second decomposition phase unfolds from 120 to 360 °C, marked by the elimination of $\text{C}_6\text{H}_7\text{Cl}_2$, reaching its zenith at 213.73 °C and leading to an observed mass loss of 26.32% (calculated = 26.54%). The third stage, spanning 360 to 735 °C, involves the decomposition of the $\text{C}_7\text{H}_7\text{N}_2\text{SCL}$ moiety, manifesting a weight loss of 32.59% (theoretical 33.02%) and exhibiting a peak at 608.62 °C. The final decomposition step, occurring between 735 and 800 °C, is characterized by the release of the $\text{C}_3\text{H}_4\text{N}_3$ molecule, resulting in a weight loss of 14.24% (calculated 14.52%) with peaks observed at 564.27 and 599.68 °C. The residue after this process is identified as Cadmium oxide (**CdO**).

Table 5: Thermogravimetric and Differential Thermogravimetric Investigations on the Characteristics Thermal Decomposition of the (ZHC) and Its Metal Complexes: An In-Depth Analysis.

Complexes	TG-range (°C)	DTG max	n *	Mass loss Estim (calcd)%	Assignment	Residues
(1)	(35-100)	98	1	3.15(3.42)	-Loss of H_2O	Fe
[Fe(ZHC)Cl ₃] \cdot H ₂ O (C ₁₆ H ₁₈ Cl ₄ FeN ₅ O ₃ S)	(100-240)	200.34	2	28.56(28.74)	-Loss of $\text{C}_7\text{H}_7\text{N}_2\text{S}$	
	(240-325)	305.39	3	16.199(16.33)	-Loss of CH_3Cl_2	
	(325-800)	(564.27, 599.68)	4	40.589(40.88)	-Loss of $\text{C}_3\text{H}_6\text{Cl}_2\text{N}_3$	
(2)	(30-110)	97	1	6.65(6.79)	-Loss of $2\text{H}_2\text{O}$	CoO
[Co(ZHC)(H ₂ O)Cl ₂] \cdot 2H ₂ O (C ₁₆ H ₂₂ Cl ₃ CoN ₅ O ₃ S)	(110-305)	(112.5, 225.8, 292.34)	2	41.85(42.31)	-Loss of $\text{C}_7\text{H}_9\text{Cl}_2\text{N}_2\text{S}$	
	(305-800)	(551.11, 591.68)	3	36.59(37.12)	-Loss of $\text{C}_{19}\text{H}_{11}\text{ClN}_3$	
(3)	(30-95)	92	1	6.308(6.73)	-Loss of $2\text{H}_2\text{O}$	CuO
[Cu(ZHC)(H ₂ O)Cl ₂] \cdot 2H ₂ O (C ₁₆ H ₂₂ Cl ₃ CuN ₅ O ₃ S)	(95-400)	(165.5, 213.59)	2	25.79(26.49)	-Loss of $\text{C}_7\text{H}_8\text{ClN}$	
	(400-800)	463.39	3	51.46(51.87)	-Loss of $\text{C}_9\text{H}_{10}\text{Cl}_2\text{N}_4\text{S}$	of
(4)	(40-120)	94	1	2.79(3.18)	-Loss of H_2O	CdO
[Cd(ZHC)(H ₂ O)Cl ₂] \cdot H ₂ O (C ₁₆ H ₂₀ CdCl ₃ N ₅ O ₂ S)	(120-360)	213.73	2	26.32(26.54)	-Loss of $\text{C}_6\text{H}_7\text{Cl}_2$	
	(360-735)	608.62	3	33.59(33.02)	-Loss of $\text{C}_7\text{H}_7\text{N}_2\text{SCL}$	
	(735-800)	711.39	4	14.24(14.52)	-Loss of $\text{C}_3\text{H}_4\text{N}_3$	

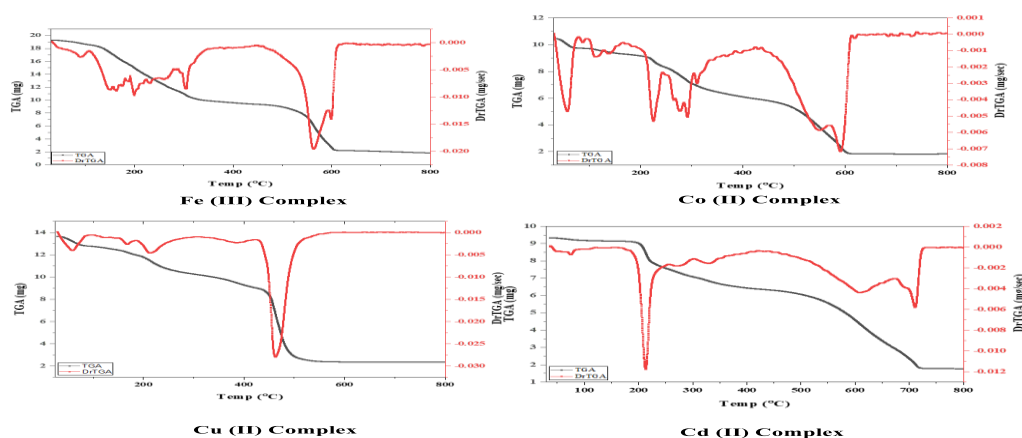


Fig 3. Thermogravimetric Analysis (TGA) of Binary ZHC-Metal Complexes

3.2.8. Structural interpretation

The structures of the unbound (ZHC) and its corresponding metal complexes were elucidated through a thorough investigation, incorporating elemental analyses, IR, ^1H NMR, mass spectrometry, UV–visible spectroscopy, molar conductance measurements, and thermal analyses involving thermogravimetric (TG) and differential thermogravimetric (DTG) analyses. The proposed structural representations of the complexes have been classified into three distinct coordination types, as illustrated in Scheme 2.

3.3. Geometry theoretical study

3.3.1. Computational Insights into the Molecular Geometry and Reactivity Descriptors: A Density Functional Theory Study

The optimization of molecular geometry was carried out utilizing Density Functional Theory (DFT), with a specific focus on the ligand (ZHC) and its Cd (II) complex, chosen due to its historically notable biological activity [1, 2, 53]. Table 6 presents the fully optimized geometries, complete with atomic numbering.

Table 6: Computational Exploration of Molecular Orbital Properties: HOMO and LUMO Analysis of the (ZHC) and its Cadmium (II) Complex Utilizing DFT Methodology.

Optimized geometry visualization of the studied (ZHC) and its Cd(II) Complex				
Compound	optimized structure	3D-HOMO	3D-LUMO	ΔE (eV)
(ZHC)				6.918 9
$[\text{Cd}(\text{ZHC})(\text{H}_2\text{O})\text{Cl}_2] \cdot \text{H}_2\text{O}$				3.182 9

Table 7: Comparative Examination of Optimized Quantum Chemical Parameters for a Schiff Base Ligand (ZHC) and Its Cadmium (II) Complexes

Quantum Chemical Parameters Computation	(ZHC)	[Cd(ZHC)(H ₂ O)Cl ₂].H ₂ O
E (a.u)	-1744.42	-1072.4803
Dipole moment (Debye)	4.3587	12.8135
E _{HOMO} (eV)	-8.188	-5.8983
E _{LUMO} (eV)	-1.2691	-2.7154
ΔE (eV)	6.9189	3.1829
η(eV)	3.45945	1.59145
χ (eV)	4.72855	4.30685
σ(eV) ⁻¹	0.28906329	0.628357787
Pi (eV)	-4.72855	-4.30685
S (eV) ⁻¹	0.144531645	0.314178893
ω(eV)	3.231609808	5.827690761
ΔN _{max}	1.366850222	2.706242735
Bond lengths (Å)	Schiff base ligand (ZHC)	[Cd(ZHC)(H₂O)Cl₂].H₂O
C(15)-N(17)	1.337	1.376
N(14)-C(15)	1.353	1.376
C(11)-N(12)	1.264	1.318
N(9)-C(10)	1.262	1.318
N(8)-N(9)	1.328	1.346
Bond angles (°)	(ZHC)	[Cd(ZHC)(H₂O)Cl₂].H₂O
Cl(27)-Cd(24)-O(26)	95.112
Cl(27)-Cd(24)-Cl(25)	149.595
Cl(27)-Cd(24)-S(16)	101.066
Cl(27)-Cd(24)-N(12)	97.99
Cl(27)-Cd(24)-N(9)	91.258
O(26)-Cd(24)-Cl(25)	74.599
O(26)-Cd(24)-S(16)	91.766
O(26)-Cd(24)-N(12)	160.578
O(26)-Cd(24)-N(9)	129.325
Cl(25)-Cd(24)-S(16)	107.673
Cl(25)-Cd(24)-N(12)	100.198
Cl(25)-Cd(24)-N(9)	74.98
S(16)-Cd(24)-N(12)	71.718
S(16)-Cd(24)-N(9)	136.006
N(12)-Cd(24)-N(9)	64.772

3.3.2. Molecular electrostatic potential (MEP)

As detailed in Table 7 [54], calculated bond lengths and angles indicate a distorted octahedral geometry around the Cd (II) ion. Supplementary Table S1 provides comprehensive data for the (ZHC) and its Cd (II) complex, encompassing bond lengths and angles. The Cd (II) complex exhibits subtle elongation in specific bond lengths, specifically C (15)-N (17), N (14)-C (15), C (11)-N (12), N (9)-C (10), N (8)-N (9). This elongation is attributed to the coordination of the (ZHC) through the involvement of two azomethine nitrogen atoms and the sulfur of the (C=S) group. The global reactivity descriptors, encompassing various parameters such as the HOMO–LUMO energy gap (ΔE), ionization potential (I), electron affinity (A), chemical potentials (μ), absolute electronegativity (χ), absolute softness (σ), global electrophilicity (ω), absolute hardness (η), global softness (S), and additional electronic charge (ΔN_{\max}) were systematically computed for both a Schiff base ligand (ZHC) and its Cd (II) complex using consistent computational methodologies. The detailed findings are presented in Table 6 [55]. The determination of these molecular properties involves specific computations, including absolute hardness ($\eta = (I - A)/2 = (E_{\text{LUMO}} - E_{\text{HOMO}})/2$), global softness (S, where $S = 1/2\eta$), chemical potential (μ , where $\mu = -(I + A)/2$), and electronegativity (χ , where $\chi = (I + A)/2 = (E_{\text{LUMO}} + E_{\text{HOMO}})/2$). The HOMO–LUMO energy gap (ΔE) is calculated as $\Delta E = E_{\text{LUMO}} - E_{\text{HOMO}}$, absolute softness (σ) as $\sigma = 1/\eta$, and additional electronic charge (ΔN_{\max}) as $\Delta N_{\max} = -I/\eta$. A reduced energy gap indicates the presence of charge transfer interactions within the molecule, influencing its biological activity. The energy gap serves as a crucial indicator of the chemical reactivity of a molecule, with a narrow frontier orbital gap suggesting heightened reactivity, classifying the molecule as "soft." This energy gap is also a significant stability index, elucidating structural and conformational barriers in various molecular systems. For the (ZHC), the energy gap was determined to be 6.9189 eV, while its Cd (II) complex was measured to be 3.1829 eV. A higher energy gap implies increased stability of the compound. The chemical potential (μ) also exhibited a negative value, while the electrophilicity index (χ) was positively valued. These observations imply that the Schiff base ligand likely functions as an electron donor to the metal ions [56].

Electrostatic potential $V(r)$ maps were computed to discern the electronic charge distribution surrounding the molecular surface to investigate molecular reactions, aiding in the prediction of potential reaction sites [1-3]. Utilizing the same basis set as optimized by Gaussian software, 3D Molecular Electrostatic Potential (MEP) maps were generated for both the (ZHC) and its Cd (II) complex (Fig 4). MEP analysis typically highlights red areas as electron-rich (favoring electrophilic attack) and blue areas as electron-deficient (favoring nucleophilic attack), while green areas signify neutral electrostatic potential. The ligand exhibits stability with an evenly distributed charge density, except for sulfur atoms, which are enveloped by a larger negatively charged surface, suggesting susceptibility to electrophilic attack (yellow) (Fig 4 A). The aromatic ring, in terms of electron density, appears neutral. This electrostatic potential distribution influences complexation reactions, a phenomenon corroborated by examining the Cd (II) complex's electrostatic potential distribution, wherein the most prominent negative charge surrounds the metal center (Fig 4 B). The Cd (II) complex exhibits an increased electron-negative capacity in sulfur and nitrogen compared to the free ligand, making these sites more favorable for electrophilic attack. This observation aligns with the Mulliken electron-negative analysis, highlighting these locations as preferred sites for interaction with the metal ion (Fig 4) [57, 58].

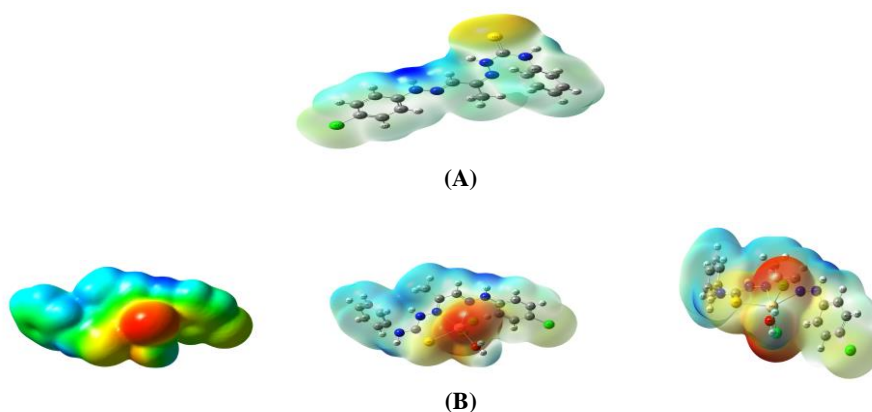


Fig 4. Molecular Electrostatic Potential Mapping for the (ZHC) and its Cadmium Complex $[\text{Cd}(\text{ZHC})(\text{H}_2\text{O})\text{Cl}_2] \cdot \text{H}_2\text{O}$: Analysis at an Electron Density Isosurface of 0.004 Atomic Units.

3.4. pharmacology study

3.4.1 Antimicrobial activities

Compared to their unbound (ZHC), the heightened antibacterial efficacy observed in metal complexes can be attributed to the chelation process. This intricate coordination involves binding the (ZHC) with metal ions, imparting both polar and nonpolar characteristics to the resultant metal chelates [59]. The mechanism by which these metal complexes exert their enhanced biological effects can be attributed to several factors. **Firstly**, the reduction in metal ion polarity induced by chelation is particularly noteworthy, driven by the overlapping ligand orbitals that partially share the metal ion's positive

charge with the donor groups [1-3]. This leads to increased delocalization of π -electrons throughout the entire chelate ring, promoting enhanced permeation of the complexes through lipid membranes [60, 61]. This improved membrane permeability allows the complexes to accumulate more effectively within microbial cells, potentially interfering with crucial cellular processes. Secondly, the chelation process alters the central metal ions' hydrophilic and lipophilic properties, enhancing their lipid solubility. This modification facilitates the complexes' passage through the lipid layer of cell membranes, a critical factor affecting the rate at which molecules traverse cell barriers [60, 62]. The increased lipophilicity may enable the complexes to interact more efficiently with intracellular targets, such as DNA or essential enzymes, leading to enhanced antimicrobial activity. Furthermore, the metal complexes may exert their biological effects through multiple mechanisms simultaneously. These could include **A**) Disruption of cell membrane integrity. **B**) Interference with metal-dependent enzymes essential for microbial survival. **C**) Generation of reactive oxygen species (ROS) that cause oxidative stress. **D**) Binding to and altering the function of crucial biomolecules such as proteins or nucleic acids. The synergistic effect of these mechanisms likely contributes to the observed superior antimicrobial activity of the metal complexes compared to the free Schiff base ligand [1]. The primary objective of any antimicrobial compound is to inhibit target microbes without causing adverse effects on patients [63]. To evaluate the efficacy of the (ZHC) and its metal complexes, assessments have been conducted against four distinct bacterial species: *Staphylococcus aureus*, *Streptococcus mutans*, *Escherichia coli*, and *Klebsiella pneumonia*. Additionally, screening was performed against the fungal strain *Candida albicans* and *Aspergillus Nigar* [64]. The biological activities of the (ZHC) and its complexes were benchmarked against standard antibacterial agents Gentamicin and Ampicillin and the antifungal agent Nystatin [65]. The results indicate that the biological activities of the complexes surpass those of the free (ZHC). Notably, Cd (II) exhibited the highest activity, while the Cu (II) and Fe (III) complexes demonstrated the lowest, although all were superior to the standard. Co (II) and Cd (II) complexes exceeded the standard in antifungal activity. Detailed outcomes of these assessments are presented in Table 8 and graphically depicted in Fig 5. The collected data underscores that the (ZHC) and its metal complexes exhibit significant biological activity against a spectrum of bacterial species, except for the Cu (II) and Fe (III) complexes, which lacked efficacy against certain bacterial and fungal strains, as delineated in Table 8. Recent studies on Schiff base complexes with Co (II) and Cu (II) have shown promising antimicrobial and anticancer properties. For instance, Mansour et al. (2024) reported Cu (II) complexes of quinolin-2(1H)-one-derived Schiff bases with MIC values ranging from 20-200 $\mu\text{g/mL}$ against various bacterial strains. In comparison, the Cu (II) complex in this study demonstrated inhibition zones of 17.7-31.7 mm against similar strains, indicating potentially superior antimicrobial activity [1, 2].

Table 8: Exploring the Bioactivity of the (ZHC) and Its Associated Metal Complexes: An Investigation into Biological Effects.

Sample	Inhibition zone diameter (mm / mg sample)					
	Gram-(-V)- bacteria		Gram-(+Ve)- bacteria		Fungus	
	<i>Escherichia coli</i>	<i>Klebsiella pneumonia</i>	<i>Staphylococcus aureus</i>	<i>Streptococcus mutans</i>	<i>Candida albicans</i>	<i>Aspergillus Nigar</i>
Control: DMSO	0	0	0	0	0	0
(ZHC)	26.8±0.5	22.3±0.5	25.1±1	24.7±0.1	19.4±0.1	26.2±0.5
[Fe(ZHC)Cl ₃].H ₂ O	13.7 ±0.5	14.6±0.6	19.8±0.6	NA	NA	18.9±1.0
[Co(ZHC)(H ₂ O)Cl ₂].2H ₂ O	21±0.5	23.2±0.5	20.5±0.1	23.8±0.5	28.6±0.5	26. ±0.5
[Cu(ZHC) (H ₂ O)Cl ₂].2H ₂ O	NA	11.3±0.5	17.8	NA	15.7±0.5	NA
[Cd(ZHC)(H ₂ O)Cl ₂].H ₂ O	29.7±0.6	27.6±	30.3±0.5	24.7±1.0	33.0±1.0	34.2±0.5
Gentamicin	27±0.5	25±0.5	-----	-----	-----	-----
Ampicillin	-----	-----	20±0.1	28±0.5	-----	-----
Nystatin	-----	-----	-----	-----	21±0.5	29±0.5

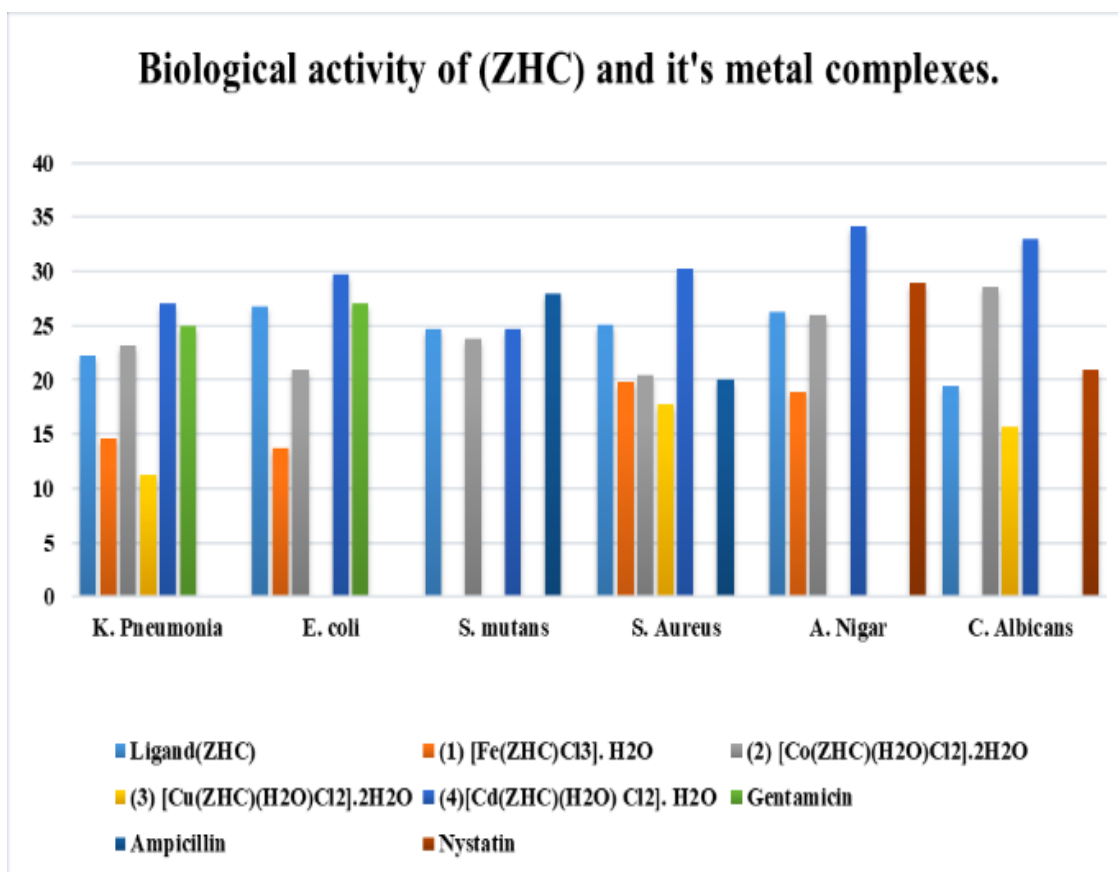


Fig 5. Antibacterial Biological Efficacy of the (ZHC) and Its Metal Complexes

3.4.2. Anticancer activities

In contemporary research within the field of pharmaceutical sciences, significant focus is directed towards exploring novel active compounds designed for cancer treatment. A particular emphasis is placed on the advancement of metal-based anti-cancer drugs. This endeavor is fundamental to synthesizing and evaluating various transition metal complexes. In the context of laboratory experimentation, *in vitro* studies were conducted to assess the cytotoxic impact of a (ZHC) and its complexes on MCF-7 (Breast carcinoma) cells. Survival curves, graphically representing the concentration-dependent relationship between the compounds and the relative viability of cells, were generated (see Fig 6). Additionally, Table 9 provides IC₅₀ values, denoting the concentration causing a 50% inhibition of cancer cell growth. The mechanisms underlying the anticancer activities of these metal complexes are likely multifaceted and may involve several interrelated processes [66, 67]:

1. **Enhanced cellular uptake:** The improved lipophilicity of the metal complexes, particularly the Cd(II) complex, may facilitate their passage through cell membranes, leading to higher intracellular concentrations and increased efficacy.
2. **DNA binding and damage:** Metal complexes can interact with DNA through intercalation, groove binding, or covalent bonding. This interaction may lead to DNA damage, inhibition of replication and transcription, and ultimately cell death.
3. **Generation of reactive oxygen species (ROS):** Many metal complexes can catalyze the production of ROS, leading to oxidative stress and cellular damage. This mechanism may be particularly relevant for the more active complexes, such as the Cd (II) complex.
4. **Enzyme inhibition:** Metal complexes may interact with and inhibit crucial enzymes involved in cell proliferation and survival, such as topoisomerases or protein kinases.
5. **Modulation of cell signaling pathways:** The complexes may interfere with cellular signaling cascades involved in cancer cell proliferation, survival, and metastasis.

Noteworthy observations regarding cytotoxicity against MCF-7 cells are summarized as follows:

A. Metal complexes of the Schiff base ligand, notably (**ZHC**), along with complexes of Fe (III), Co (II), Cu (II), and Cd (II), exhibited significant efficacy towards cancer cells, with respective IC_{50} values of 12.5, 55, 15, 21, and 10 $\mu\text{g/mL}$. These findings position these compounds as promising candidates in chemotherapy, with IC_{50} reflecting the concentration causing a 50% inhibition in cancer cell growth.

B. The potency sequence concerning the chelated metal ions with the ligand follows the order: **Fe (III)** < **Cu (II)** < **Co (II)** < (**ZHC**) < **Cd (II)** against MCF-7 cells.

C. Comparative analysis of the free (**ZHC**) antitumor activities and its metal complexes reveals that the Cd-complex demonstrates superior antitumor activity compared to the ligand and other metal complexes (see Table 9).

D. Fe (III) metal complex displayed minimal cytotoxic effects on all investigated cancer cell lines, while the Cd (II) complex exhibited notably cytotoxic solid effects.

E. A distinct correlation is observed between antitumor activities and antimicrobial activities. For instance, the Cd-complex displayed elevated antifungal and antibacterial activity against investigated fungal and bacterial species (refer to Table 8), in addition to robust antitumor activities against MCF-7 (Breast carcinoma) cells (refer to Table 9).

F. The complex $[\text{Cd}(\text{ZHC})(\text{H}_2\text{O})\text{Cl}_2]\cdot\text{H}_2\text{O}$ has been identified as the most potent and effective candidate for a breast cancer anticancer drug among the prepared compounds. This increased activity is likely due to the presence of the azomethine group within the macrocyclic chelate ring. When metal ions coordinate with the nitrogen in the azomethine group, it appears to reduce the metal atoms' polarity, possibly because the positive charge is partially shared with the ligand [68–70]. Additionally, the activity might be enhanced due to greater π -electron delocalization in the ligand when the complex forms. This could improve the compounds' ability to penetrate cell membranes' lipid layers and thus increase their overall efficacy [71].

In terms of anticancer properties, Ali et al. (2024) synthesized Schiff base ligand and its Cu(II) complexes that showed IC_{50} values of 372.99 and 322.80 $\mu\text{g/mL}$, respectively, against MCF-7 cells [72]. The current study's Schiff base ligand and its Cu (II) complex exhibited IC_{50} values of 12.5 and 21 $\mu\text{g/mL}$, respectively, which, while less potent, still demonstrate significant anticancer potential.

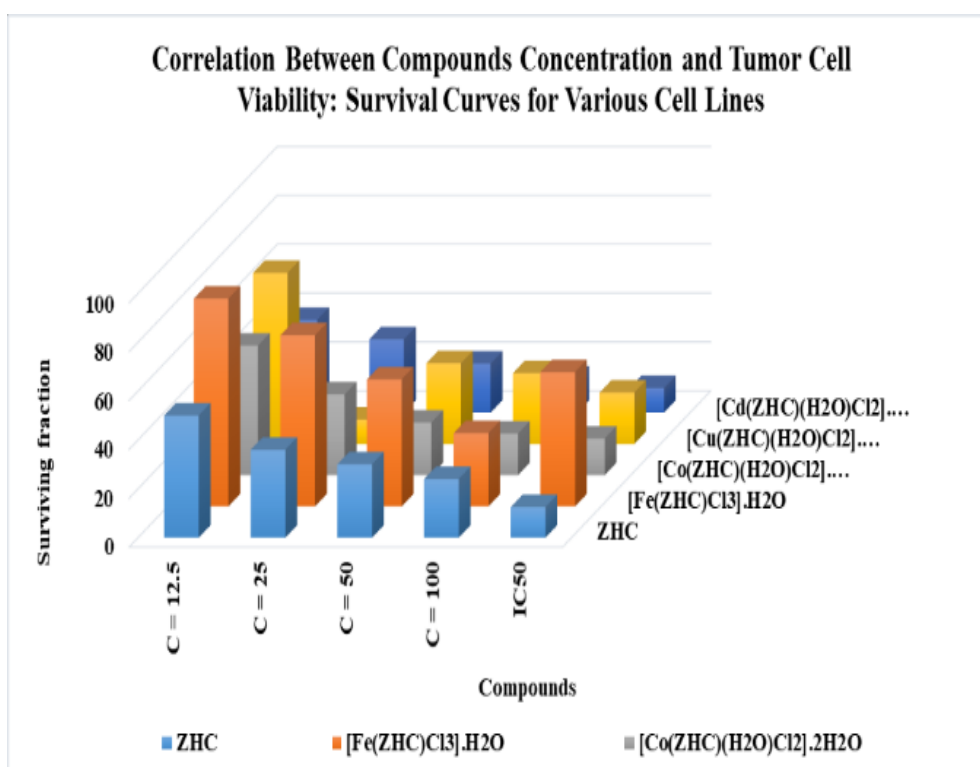


Fig 6. Anticancer Efficacy on Breast Cancer of (**ZHC**) and Its Metal Complexes

Table 9: Anticancer Efficacy Targeting Breast Cancer: Evaluation of (ZHC) and Its Metal Complexes

Sample	Concentration ($\mu\text{g/mL}$)				IC_{50} ($\mu\text{g/mL}$)
	12.5	25	50	100	
	Surviving fraction (MCF-7)				
(ZHC)	50	36	30	24	12.5
(1) [Fe(ZHC)Cl ₃] \cdot H ₂ O	85	70	52	30	55
(2) [Co(ZHC)(H ₂ O)Cl ₂] \cdot 2H ₂ O	53	33	21.5	17	15
(3) [Cu(ZHC)(H ₂ O)Cl ₂] \cdot 2H ₂ O	70	40	33	29	21
(4) [Cd(ZHC)(H ₂ O)Cl ₂] \cdot H ₂ O	38	30	20	14	10

A) The IC_{50} , denominated in micrograms per milliliter ($\mu\text{g/ml}$), signifies the concentration of a pharmacological agent required to achieve a 50% inhibition of cancer cell proliferation, indicating its cytotoxic efficacy.

B) The IC_{50} spectrum, quantified in micrograms per milliliter ($\mu\text{g/ml}$), categorizes the drug's effectiveness into discrete ranges: 1-10 (high potency), 11-20 (potent), 21-50 (moderate potency), 51-100 (mild potency), and exceeding 100 (non-cytotoxic) [73].

C) Specifically concentrating on MCF-7, a subtype of breast carcinoma cell line

3.5. Docking study of the (ZHC) and its [Cd(ZHC)(H₂O)Cl₂] \cdot H₂O complex.

An investigation was initiated to explore potential binding sites for the (ZHC) and its Cd (II) complex within two distinct receptors. These receptors included Human topoisomerase IIbeta complexed with DNA and etoposide (**PDB ID: 3QX3**) [30], integral components in cancer treatment, and the Main Protease (Mpro) of SARS-CoV-2, a crucial antiviral drug target, represented by the Crystal structure of the SARS-CoV-2 (COVID-19) main protease in complex with inhibitor UAW247 (**PDB ID: 6XBH**) [31]. Computational analysis was conducted using MOE 2014.09 software, predicting the binding mode within protein pockets. The program operated on an Intel Pentium 1.6-GHz processor with 512-MB memory, running on the Windows XP operating system. Minimizations were performed with MOE until an RMSD gradient of 0.05 KCal/mol \AA using the MMFF94X force field, and automatic calculation of partial charges was implemented [72]. Docking results for the (ZHC) and its Cd (II) complex are presented in both two-dimensional (2D) and three-dimensional (3D) plots, detailed in Tables 12, respectively. Additionally, binding energies for the (ZHC) and its Cd (II) complex are provided in Tables 10 and 11. Consistent with experimental findings, the Schiff base ligand (ZHC) exhibited a significant IC_{50} value of 12.5 $\mu\text{g/ml}$ when assessed against a breast cancer cell line. Furthermore, the Cadmium (II) complex [Cd(ZHC)(H₂O)Cl₂] \cdot H₂O, derived from the abovementioned ligand, demonstrated enhanced anticancer efficacy with lower IC_{50} values of 10 $\mu\text{g/ml}$. To support these outcomes, theoretical docking investigations focused on the receptors of Human topoisomerase IIbeta in complex with DNA and etoposide (**PDB ID: 3QX3**). Human topoisomerase is the molecular target for a diverse array of anticancer compounds. The docking analysis results indicated that the Schiff base ligand (ZHC) and its Cadmium (II) complex, denoted as [Cd(ZHC)(H₂O)Cl₂] \cdot H₂O, exhibited notably low binding energies of -2.8 and -11.2 kcal mol⁻¹, respectively, suggesting heightened activity in the complexes compared to the parent ligand, attributed to forming coordination bonds with the Cadmium (II) metal ion. A more in-depth examination of the interactions of these compounds with the protein receptor of the SARS-CoV-2 (COVID-19) revealed substantial and compelling interactions, as detailed in Tables (10 and 11) [74]. Predominantly observed interaction forces included H-donor, H-acceptor, ionic, and π -H interactions. The (ZHC) and its Cd (II) complex, associated with receptors **3QX3** and **6XBH**, manifested distinct binding energies. Specifically, the lowest binding energies were determined as -2.8 and -2.4 kcal mol⁻¹ for the (ZHC). At the same time, the Cd (II) complex exhibited binding energies of -11.2 and -8.2 kcal mol⁻¹ with the respective receptors. Notably, the coordination process resulted in a discernible reduction in binding energy [72]. Consequently, the Cd (II) complex demonstrated heightened activity compared to the (ZHC), indicating its potential efficacy as a promising therapeutic agent against gastroenteritis in prospective applications.

Table 10: Calculated Interaction Energies: Docking Assessment of (ZHC) with Diverse Protein Receptors Linked to Cancer Cells and COVID-19

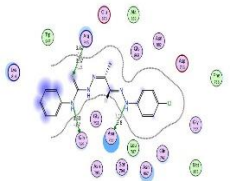
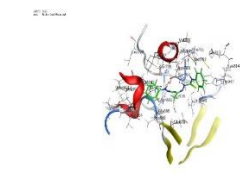
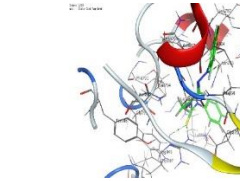
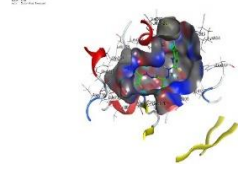
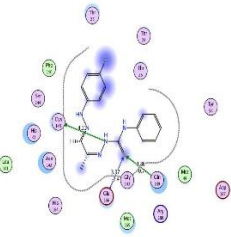
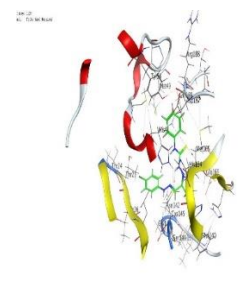
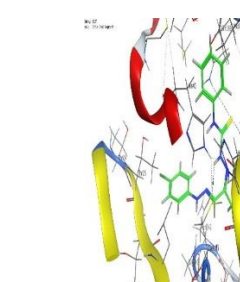
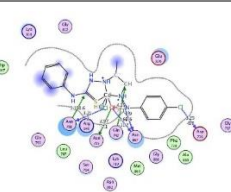
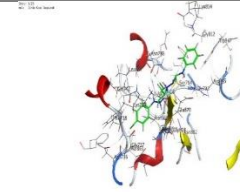
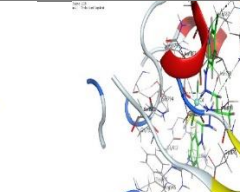
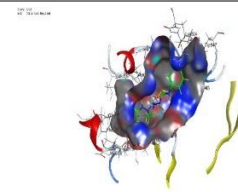
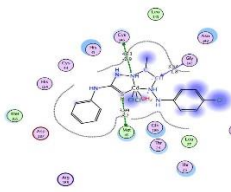
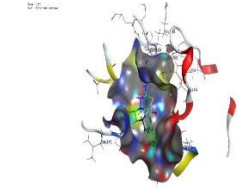
Type	Receptor	Ligand moiety	Receptor site	Interaction	Distance (Å°)	E (kcal/mol)
Cancer cells	3QX3	N 8	OD1 ASN 786 (A)	H-donor	3.18	-2.8
		N 17	OE1 GLN 789 (A)	H-donor	3.33	-1.7
		S 16	NE ARG 945 (A)	H-acceptor	3.87	-1.2
COVID 19	6XBH	S 16	NH2 ARG 945 (A)	H-acceptor	3.57	-1.5

Table 11: Evaluating Interaction Energies Arising from Docking Simulations of a Cd (II) Complex with Diverse Protein Receptors Linked to Oncogenic Cells and COVID-19.

Type	Receptor	Ligand moiety	Receptor site	Interaction	Distance (Å°)	E (kcal/mol)
Cancer cells	3QX3	CL 7	O ASP 736 (A)	H-donor	3.25	-0.6
		N 9	O ASN 867 (A)	H-donor	2.90	-2.6
		CI 28	O ASN 786 (A)	H-donor	3.21	-2.0
		O 29	OD1 ASN 795 (A)	H-donor	2.97	-7.1
		O 29	O ASN 867 (A)	H-donor	2.69	-11.2
		C 11	NE2 GLN 742 (A)	H-acceptor	4.35	-1.1
		C 17	ND2 ASN 786 (A)	H-acceptor	3.15	-0.6
		COVID 19	6XBH	N 13	SG CYS 145 (A)	H-donor
		S 18	SD MET 49 (A)	H-donor	3.99	-8.2
		C 11	N GLY 143 (A)	H-acceptor	3.54	-1.8

Table 12: Molecular docking 2D and 3D for predicting the possible binding modes of the studied (ZHC) and its $[\text{Cd}(\text{ZHC})(\text{H}_2\text{O})\text{Cl}_2]\cdot\text{H}_2\text{O}$ complex, with the receptors of the crystal structure from Protein Data Bank of different types of receptors (3QX3 and 6XBH).

Schiff base ligand (ZHC) interaction with a specific protein receptor

Receptor (organism)	2D Ligand interaction	3D Ligand interaction		
		Center view	Isolated view	View inside pocket on the surface of receptor protein
Cancer cells (3QX3)				
COVID 19 (6XBH)				
$[\text{Cd}(\text{ZHC})(\text{H}_2\text{O})\text{Cl}_2]\cdot\text{H}_2\text{O}$				
Cancer cells (3QX3)				
COVID 19 (6XBH)				

4. Conclusion

This investigation comprehensively analyses a tridentate Schiff base ligand (denoted as ZHC) and its corresponding metal complexes. Various analytical techniques have been employed for thorough characterization, including elemental analysis, molar conductance, mass spectroscopy, ^1H NMR, magnetic susceptibility, infrared (IR), and UV-visible spectroscopy. The outcomes of these analyses elucidated the formation of octahedral-shaped complexes, specifically $[\text{Fe}(\text{ZHC})\text{Cl}_3]\cdot\text{H}_2\text{O}$, $[\text{Co}(\text{ZHC})(\text{H}_2\text{O})\text{Cl}_2]\cdot 2\text{H}_2\text{O}$, $[\text{Cu}(\text{ZHC})(\text{H}_2\text{O})\text{Cl}_2]\cdot 2\text{H}_2\text{O}$, and $[\text{Cd}(\text{ZHC})(\text{H}_2\text{O})\text{Cl}_2]\cdot\text{H}_2\text{O}$. The antimicrobial assessment revealed that the $[\text{Cd}(\text{ZHC})(\text{H}_2\text{O})\text{Cl}_2]\cdot\text{H}_2\text{O}$ complex exhibited significantly elevated toxicity against both bacterial and fungal species. Furthermore, the Schiff base metal complex investigated in this study demonstrated substantial activity against MCF-7 (Breast carcinoma), indicating its potential for diverse biological activities. These findings underscore the promise of these compounds for further exploration in medicinal and pharmaceutical research.

References

1. Mansour MS, Ibrahim AT, El-Sherif AA, Mahmoud WH. Organotin (IV) complexes: Synthesis, characterization, DFT, and molecular docking studies unveiling their potential biomedical uses. *Appl Organomet Chem* [Internet]. 2024 Aug 11;n/a(n/a):e7656. 1. Mansour MSA, Abdelkarim AT, El-Sherif AA, Mahmoud WH. Metal complexes featuring a quinazoline Schiff base ligand and glycine: synthesis, characterization, DFT and molecular docking analyses revealing their potent antibacterial, anti-helicobacter pylori, and anti-COVID-19 activities. *BMC Chem.* 2024;18(1).
2. M. S. A. Mansour, A. T. Abd-Elkarim, W. H. Mahmoud, and A. A. El-Sherif, "Quinazoline-Glycine Manganese (II) Nano-Complex for Arsenic Sensing via QCM: Synthesis, Characterization, DFT Studies, Biological Evaluation, and Environmental Application," *Egypt. J. Chem.*, 2024.
3. H. M. Fahmy, F. M. Abdel-Rahman, A. A. El-Sayed, and A. A. El-Sherif, "Study of novel bidentate heterocyclic amine-based metal complexes and their biological activities: cytotoxicity and antimicrobial activity evaluation," *BMC Chem.*, vol. 17, no. 1, p. 78, 2023.
4. O. M. Fahmy, W. H. Mahmoud, R. M. El Nashar, and A. A. El-Sherif, "Nano Co (II) and Pd (II) Schiff base Complexes: Structural Characterization, Molecular docking, Antitumor proficiency and Biological evaluation," *Egypt. J. Chem.*, vol. 66, no. 13, pp. 1373–1382, 2023.
5. A. M. Abu-Dief, L. H. Abdel-Rahman, M. R. Shehata, and A. A. H. Abdel-Mawgoud, "Novel azomethine Pd (II)-and VO (II)-based metallo-pharmaceuticals as anticancer, antimicrobial, and antioxidant agents: Design, structural inspection, DFT investigation, and DNA interaction," *J. Phys. Org. Chem.*, vol. 32, no. 12, p. e4009, 2019.
6. E. T. Aljohani, M. R. Shehata, F. Alkhatib, S. O. Alzahrani, and A. M. Abu-Dief, "Development and structure elucidation of new VO₂⁺, Mn²⁺, Zn²⁺, and Pd²⁺ complexes based on azomethine ferrocenyl ligand: DNA interaction, antimicrobial, antioxidant, anticancer activities, and molecular docking," *Appl. Organomet. Chem.*, vol. 35, no. 5, p. e6154, 2021.
7. A. M. Abu-Dief, H. M. El-Sagher, and M. R. Shehata, "Fabrication, spectroscopic characterization, calf thymus DNA binding investigation, antioxidant and anticancer activities of some antibiotic azomethine Cu (II), Pd (II), Zn (II) and Cr (III) complexes," *Appl. Organomet. Chem.*, vol. 33, no. 8, p. e4943, 2019.
8. M. S. Aljahdali and A. A. El-Sherif, "Synthesis and biological evaluation of novel Zn (II) and Cd (II) Schiff base complexes as antimicrobial, antifungal, and antioxidant agents," *Bioinorg. Chem. Appl.*, vol. 2020, no. 1, p. 8866382, 2020.
9. H. Muğlu, "Synthesis, characterization, and antioxidant activity of some new N 4-arylsubstituted-5-methoxyisatin- β -thiosemicarbazone derivatives," *Res. Chem. Intermed.*, vol. 46, pp. 2083–2098, 2020.
10. M. Bingul, E. Şenkuytu, M. F. Saglam, M. Boga, H. Kandemir, and I. F. Sengul, "Synthesis, photophysical and antioxidant properties of carbazole-based bis-thiosemicarbazones," *Res. Chem. Intermed.*, vol. 45, pp. 4487–4499, 2019.
11. J. M. Mir, S. A. Majid, and A. H. Shalla, "Enhancement of Schiff base biological efficacy by metal coordination and introduction of metallic compounds as anticovid candidates: a simple overview," *Rev. Inorg. Chem.*, vol. 41, no. 4, pp. 199–211, 2021.
12. R. K. Mohapatra et al., "Synthesis, structural investigations, DFT, molecular docking and antifungal studies of transition metal complexes with benzothiazole based Schiff base ligands," *J. Mol. Struct.*, vol. 1179, pp. 65–75, 2019.
13. C. Boulechfar et al., "Schiff bases and their metal Complexes: A review on the history, synthesis, and applications," *Inorg. Chem. Commun.*, vol. 150, p. 110451, 2023.
14. M. I. Khan, S. Gul, and M. A. Khan, "Schiff bases and their metallic derivatives: highly versatile molecules with biological and abiological perspective," in *Stability and Applications of Coordination Compounds*, IntechOpen, 2019.
15. R. Kumar et al., "Synthesis, antibacterial and antifungal activities of Schiff base rare earth metal complexes: a review of recent work," *J. Coord. Chem.*, vol. 76, no. 9–10, pp. 1065–1093, 2023.
16. P. Varma, "Synthesis and characterization of metal complexes with chelating ligands." Department of Chemistry, University of Calicut, 2018., 2018.

17. J. Karges, R. W. Stokes, and S. M. Cohen, "Metal complexes for therapeutic applications," *Trends Chem.*, vol. 3, no. 7, pp. 523–534, 2021.
18. K. J. Franz and N. Metzler-Nolte, "Introduction: metals in medicine," *Chemical Reviews*, vol. 119, no. 2. ACS Publications, pp. 727–729, 2019.
19. H. M. Fahmy, A. M. Mosleh, A. A. El-Sayed, and A. A. El-Sherif, "Novel palladium (II) and Zinc (II) Schiff base complexes: Synthesis, biophysical studies, and anticancer activity investigation," *J. Trace Elem. Med. Biol.*, vol. 79, p. 127236, 2023.
20. A. A. El-Sherif, A. Fetoh, Y. K. Abdulhamed, and G. M. A. El-Reash, "Synthesis, structural characterization, DFT studies and biological activity of Cu (II) and Ni (II) complexes of novel hydrazone," *Inorganica Chim. Acta*, vol. 480, pp. 1–15, 2018.
21. R. Dennington, T. Keith, and J. Millam, "GaussView, Version 4.1. 2," Semicem Inc., Shawnee Mission. KS, 2007.
22. M. Frisch, "gaussian 09, Revision d. 01, Gaussian," Inc, Wallingford CT, vol. 201, 2009.
23. P. A. Khalaf-Alla, M. M. Shoukry, M. R. Shehata, A. M. Abdel Wahab, and R. Van Eldik, "Synthesis, equilibrium, DFT, and docking studies of a homopiperazine complex with dibutyltin(IV)," *Journal of Coordination Chemistry*, vol. 77(7-8), pp. 880-895, 2024.
24. A. W. Bauer, W. M. M. Kirby, J. C. Sherris, and M. Turck, "Antimicrobial investigations," *Am. J. Clin. Pathol*, vol. 45, pp. 493–496, 1966.
25. Y. M. Ahmed, W. H. Mahmoud, M. M. Omar, and G. G. Mohamed, "Synthesis, characterization and biological activity of transition metals schiff base complexes derived from 4, 6-Diacetylresorcinol and 1, 8-Naphthalenediamine," *J. Inorg. Organomet. Polym. Mater.*, vol. 31, pp. 2339–2359, 2021.
26. A. Bauer, W. M. M. Kirby, and J. C. Sherris, "turck, Turck M. Antibiotic susceptibility testing by a standardized single disk method," *Am. J. Clin. Pathol.*, vol. 45, no. 4, p. 493, 1966.
27. A. C. Scott, "Laboratory control of antimicrobial therapy," *Pract. Med. Microbiol.*, vol. 13, pp. 161–181, 1989.
28. P. Skehan *et al.*, "New colorimetric cytotoxicity assay for anticancer-drug screening," *JNCI J. Natl. Cancer Inst.*, vol. 82, no. 13, pp. 1107–1112, 1990.
29. A. D. Etoposide, "Stru ctural Basis of Type II Topoisomerase Inhibition by the," *Proc. Natl. Acad. Sci. USA*, vol. 102, p. 3703, 2005.
30. M. D. Sacco *et al.*, "Structure and inhibition of the SARS-CoV-2 main protease reveal strategy for developing dual inhibitors against Mpro and cathepsin L," *Sci. Adv.*, vol. 6, no. 50, p. eabe0751, 2020.
31. M. S. Mansour, W. H. Mahmoud, and A. A. El-Sherif, "Manganese, Cobalt, and Cadmium Complexes of Quinazoline Schiff Base Ligand and Methionine: Synthesis, Characterization, DFT, Docking studies and biomedical application," *Egypt. J. Chem.*, 2024.
32. A. K. Gautam, A. Kumar, K. Sharma, and B. K. Rai, "Synthesis and structural characterization of Schiff base ligand and their metal complexes," *Orient. J. Chem.*, vol. 32, no. 2, p. 1249, 2016.
33. S. M. Emam, S. Bondock, and A. A. M. Aldaloo, "Schiff base coordination compounds including thiosemicarbazide derivative and 4-benzoyl-1, 3-diphenyl-5-pyrazolone: Synthesis, structural spectral characterization and biological activity," *Results Chem.*, vol. 5, p. 100725, 2023.
34. E. M. Zayed, E. H. Ismail, G. G. Mohamed, M. M. H. Khalil, and A. B. Kamel, "Synthesis, spectroscopic and structural characterization, and antimicrobial studies of metal complexes of a new hexadentate Schiff base ligand. Spectrophotometric determination of Fe (III) in water samples using a recovery test," *Monatshefte für Chemie-Chemical Mon.*, vol. 145, pp. 755–765, 2014.
35. A. Frisch, A. B. Nielson, and A. J. Holder, "Gaussview user manual," *Gaussian Inc., Pittsburgh, PA*, vol. 556, 2000.
36. H. E. L. Ouafy, M. Aamor, M. Oubenali, M. Mbarki, A. E. L. Haimouti, and T. E. L. Ouafy, "Molecular Structure, electrostatic potential and HOMO, LUMO studies of 4-aminoaniline, 4-nitroaniline and 4-isopropylaniline by DFT," *Sci. Technol. Asia*, pp. 9–19, 2022.
37. G. R. Subhashree *et al.*, "In vitro antioxidant, antiinflammatory and in silico molecular docking studies of thiosemicarbazones," *J. Mol. Struct.*, vol. 1145, pp. 160–169, 2017.
38. A. A. El-Sherif, M. M. Shoukry, and M. M. A. Abd-Elgawad, "Protonation equilibria of some selected α -amino acids in DMSO–water mixture and their Cu (II)-complexes," *J. Solution Chem.*, vol. 42, pp. 412–427, 2013.
39. K. Mohammadi, S. S. Azad, and A. Amoozegar, "New tetradentate Schiff bases of 2-amino-3, 5-dibromobenzaldehyde with aliphatic diamines and their metal complexes: Synthesis, characterization and thermal stability," *Spectrochim. Acta Part A Mol. Biomol. Spectrosc.*, vol. 146, pp. 221–227, 2015.
40. G. R. Subhashree *et al.*, "In vitro antioxidant, antiinflammatory and in silico molecular docking studies of thiosemicarbazones," *J. Mol. Struct.*, vol. 1145, pp. 160–169, 2017.
41. K. H. D. Reddy, S.-M. Lee, K. Seshaiiah, and R. K. Babu, "Synthesis, characterization of thiosemicarabzone metal complexes and antioxidant activity in different in vitro model systems," *J. Serbian Chem. Soc.*, vol. 78, no. 2, pp. 229–240, 2013.
42. S. İlhan, "Synthesis and spectral studies of new macrocyclic Schiff base Cu (II), Ni (II), Cd (II), Zn (II), Pb (II), and La (III) complexes containing pyridine head unit," *Russ. J. Coord. Chem.*, vol. 35, no. 5, pp. 347–351, 2009.

43. M. S. A. Mansour, A. T. Abd-Elkarim, W. H. Mahmoud, and A. A. El-Sherif, "Quinazoline-Glycine Manganese (II) Nano-Complex for Arsenic Sensing via QCM: Synthesis, Characterization, DFT Studies, Biological Evaluation and Environmental Application," *Egypt. J. Chem.*, 2024.
44. Jain, A. K., Singh, R. K., Jain, S., & Raisoni, J. (2008). Copper (II) ion selective electrode based on a newly synthesized Schiff-base chelate. *Transition Metal Chemistry*, 33, 243–249.
45. Mohamed, G. G., Omar, M. M., & Ibrahim, A. A. (2009). Biological activity studies on metal complexes of novel tridentate Schiff base ligand. *Spectroscopic and thermal characterization. European Journal of Medicinal Chemistry*, 44(12), 4801–4812.
46. K. D. Patel and H. S. Patel, "Synthesis, spectroscopic characterization and thermal studies of some divalent transition metal complexes of 8-hydroxyquinoline," *Arab. J. Chem.*, vol. 10, pp. S1328–S1335, 2017.
47. L. Bellamy, *The infra-red spectra of complex molecules*. Springer Science & Business Media, 2013.
48. M. S. Refat and G. G. Mohamed, "Ti (IV), Cr (III), Mn (II), and Ni (II) complexes of the norfloxacin antibiotic drug: spectroscopic and thermal characterizations," *J. Chem. Eng. Data*, vol. 55, no. 9, pp. 3239–3246, 2010.
49. M. Refat et al., "Spectroscopic, thermal and kinetic studies of coordination compounds of Zn (II), Cd (II) and Hg (II) with norfloxacin," *J. Therm. Anal. Calorim.*, vol. 102, no. 1, pp. 225–232, 2010.
50. A. A. El-Sherif and T. M. A. Eldebss, "Synthesis, spectral characterization, solution equilibria, in vitro antibacterial and cytotoxic activities of Cu (II), Ni (II), Mn (II), Co (II) and Zn (II) complexes with Schiff base derived from 5-bromosalicylaldehyde and 2-aminomethylthiophene," *Spectrochim. Acta Part A Mol. Biomol. Spectrosc.*, vol. 79, no. 5, pp. 1803–1814, 2011.
51. A. A. El-Sherif and W. H. Mahmoud, "Mixed pd (II) complexes based on Cefadroxil drug: synthesis, characterization and biomedical applications," *Egypt. J. Chem.*, vol. 67, no. 6, pp. 353–361, 2024.
52. H. B. Schlegel, "Optimization of equilibrium geometries and transition structures," *Adv. Chem. Phys. Ab Initio Methods Quantum Chem. Part I*, vol. 67, pp. 249–286, 1987.
53. M. A. E. A. A. Ali El-Remaily et al., "Development of new thiazole complexes as powerful catalysts for synthesis of pyrazole-4-carbonitrile derivatives under ultrasonic irradiation condition supported by DFT studies," *ACS omega*, vol. 6, no. 32, pp. 21071–21086, 2021.
54. P. Tyagi, M. Tyagi, S. Agrawal, S. Chandra, H. Ojha, and M. Pathak, "Synthesis, characterization of 1, 2, 4-triazole Schiff base derived 3d-metal complexes: Induces cytotoxicity in HepG2, MCF-7 cell line, BSA binding fluorescence and DFT study," *Spectrochim. Acta Part A Mol. Biomol. Spectrosc.*, vol. 171, pp. 246–257, 2017.
55. A. Abdou, H. M. Mostafa, and A.-M. M. Abdel-Mawgoud, "Seven metal-based bi-dentate NO azocoumarine complexes: Synthesis, physicochemical properties, DFT calculations, drug-likeness, in vitro antimicrobial screening and molecular docking analysis," *Inorganica Chim. Acta*, vol. 539, p. 121043, 2022.
56. M. M. Khowdiary, N. A. Taha, A. A. Barqawi, A. A. Elhenawy, M. Sheta, and N. Hassan, "Theoretical and experimental evaluation of the anticorrosion properties of new Coumarin's derivatives," *Alexandria Eng. J.*, vol. 61, no. 9, pp. 6937–6948, 2022.
57. M. R. Shehata, M. M. Shoukry, and M. A. Mabrouk, "Metal Complexes of 1, 4-Bis (2-Hydroxyethyl) Piperazine: Thermodynamic and Theoretical Approach," *Egypt. J. Chem.*, vol. 66, no. 10, pp. 389–401, 2023.
58. S. S. Jawoor, S. A. Patil, and S. S. Toragalmath, "Synthesis and characterization of heteroleptic Schiff base transition metal complexes: a study of anticancer, antimicrobial, DNA cleavage and anti-TB activity," *J. Coord. Chem.*, vol. 71, no. 2, pp. 271–283, 2018.
59. N. Vamsikrishna, S. Daravath, N. Ganji, and N. Pasha, "Synthesis, structural characterization, DNA interaction, antibacterial and cytotoxicity studies of bivalent transition metal complexes of 6-aminobenzothiazole Schiff base," *Inorg. Chem. Commun.*, vol. 113, p. 107767, 2020.
60. N. N. Rao, K. Gopichand, R. Nagaraju, A. M. Ganai, and P. V. Rao, "Design, synthesis, spectral characterization, DNA binding, photo cleavage and antibacterial studies of transition metal complexes of benzothiazole Schiff base," *Chem. Data Collect.*, vol. 27, p. 100368, 2020.
61. W. Zafar, M. Ashfaq, and S. H. Sumrra, "A review on the antimicrobial assessment of triazole-azomethine functionalized frameworks incorporating transition metals," *J. Mol. Struct.*, p. 135744, 2023.
62. P. Garg, G. Kaur, and G. R. Chaudhary, "Metal-Embedded Complexes: Accelerated Antimicrobial Activity Against Microorganisms," in *Biomedical Research, Medicine, and Disease*, CRC Press, 2023, pp. 483–500.
63. Y. Lin, H. Betts, S. Keller, K. Cariou, and G. Gasser, "Recent developments of metal-based compounds against fungal pathogens," *Chem. Soc. Rev.*, vol. 50, no. 18, pp. 10346–10402, 2021.
64. S. S. Patil, S. K. Tadavi, A. M. Ghatole, and R. S. Bendre, "Transition metal complexes of pyridazine-based ligand: synthesis, characterization, biological activities, and molecular docking studies," *J. Iran. Chem. Soc.*, vol. 20, no. 12, pp. 3103–3117, 2023.
65. Ma K, Xu S, Tao T, Qian J, Cui Q, Rehman S ur, et al. Magnetosome-inspired synthesis of soft ferrimagnetic nanoparticles for magnetic tumor targeting. *Proc Natl Acad Sci*. 2022;119(45):e2211228119.
66. Tao T, ur Rehman S, Xu S, Zhang J, Xia H, Guo Z, et al. Biomimetic Camouflaged Metal organic framework for enhanced siRNA Delivery in Tumor Environment. *J Mater Chem B*. 2024;

67. T. A. Khan, S. Naseem, R. Hajra, and M. Shakir, "Synthesis, Physicochemical, and Antimicrobial Screening Studies of Complexes of Co (II), Ni (II), Cu (II), and Zn (II) with 18-membered Schiff Base Octaazamacrocyclic Ligand," *Synth. React. Inorganic, Met. Nano-Metal Chem.*, vol. 40, no. 10, pp. 861–868, 2010.
68. F. A. Cotton, G. Wilkinson, C. A. Murillo, and M. Bochmann, *Advanced inorganic chemistry*. John Wiley & Sons, 1999.
69. H. Zafar et al., "Synthesis and characterization of Schiff base octaazamacrocyclic complexes and their biological studies," *J. Photochem. Photobiol. B Biol.*, vol. 142, pp. 8–19, 2015.
70. H. A. El-Boraey and A. A. Serag El-Din, "Transition metal complexes of a new 15-membered [N5] pentaazamacrocyclic ligand with their spectral and anticancer studies," *Spectrochim. Acta Part A Mol. Biomol. Spectrosc.*, vol. 132, pp. 663–671, Nov. 2014.
71. Mohamed AA, El-Sherif R, Mahmoud WH, El-Sherif AA. Synthesis, Characterization, and Multifaceted Applications of Co (II) and Cu (II) Hydrazono Schiff Base Complexes: Integrating DFT, Molecular Docking, Biomedical Studies, and Nanotechnology-Enhanced Cadmium Detection Using Hydrazono Copper Complex-Base. *Egypt J Chem*. 2024;
72. T. Mosmann, "Rapid colorimetric assay for cellular growth and survival: application to proliferation and cytotoxicity assays," *J. Immunol. Methods*, vol. 65, no. 1–2, pp. 55–63, 1983.
73. Tao T, Li Z, Xu S, Rehman S ur, Chen R, Xu H, et al. Boosting SARS-CoV-2 Enrichment with Ultrasmall Immunomagnetic Beads Featuring Superior Magnetic Moment. *Anal Chem*. 2023;95(30):11542–9.